SPATIO-TEMPORAL TURBULENT CHARACTERIZATION OF A NUCLEAR REACTOR FUEL ASSEMBLY WITH SPACER GRID

A Dissertation

by

GIACOMO BUSCO

Submitted to the Office of Graduate and Professional Studies of
Texas A&M University
in partial fulfillment of the requirements for the degree of

DOCTOR OF PHILOSOPHY

Chair of Committee,	Yassin A. Hassan
Committee Members,	N.K. Anand
	Thien Duy Nguyen
	Rodolfo Vaghetto
Head of Department,	Michael Nastasi

December 2020

Major Subject: Nuclear Engineering

ABSTRACT

The present work will illustrate a series of numerical studies, performed to evaluate the predictive capabilities of various turbulence modeling approaches, applied to a typical pressurized water reactor spacer grid, with mixing vanes. Physical insight into the turbulent spatio-temporal structure of the flow will be addressed. Results will be taken as a reference for the explanation of the performances of the eddy viscosity-based turbulence models results already present in the scientific literature. Emphasis will be given to the predictive capabilities of the variable resolution (VR) turbulence models by the use of the partially averaged Navier-Stokes equations (PANS), Reynolds averaged Navier-Stokes equations (RANS) and large eddy simulation (LES). For the latter case an invariant analysis of the Reynolds stress anisotropy tensor will been conducted, based on the Lumley's triangle. This has proven to be a powerful graphical representation of the second-order statistics collection provided by the Reynolds stress tensor. A numerical solution verification and validation (V&V) metric will be suggested for the application of turbulent PANS model in nuclear reactor applications. The aforementioned set of results will contribute to an invaluable resource to further refine RANS turbulence models, deepen the understanding of the physics in this class of flows and will have the potential to lead to a better understanding of the effects of the mixing vanes and their design optimization.

DEDICATION

A mia Madre, mio Padre e mio Fratello.

Ai miei Nonni e tutta la mia Famiglia.

"An American Dream"

My journey began in an unfamiliar country with lost baggage, a missed bus connection, and a couple hundred dollars in my pocket. It will end with the same cultural confusion, just about the same amount in my pocket, in the middle of a global pandemic, but with a PhD in Nuclear Engineering.

Mocc' a kitemmurt,

Giacomo

ACKNOWLEDGEMENTS

I would like to express my sincere gratitude to my advisor Dr. Yassin Hassan. He formally asked me to join his research group in our department parking lot at Texas A&M University during the summer of 2016. Ever since that day, I never lost his continuous support, motivation, his incredible curiosity and contagious enthusiasm … especially with 4am emails and during weekends. His guidance helped me throughout the duration of my studies and research at Texas A&M University. I could not have imagined a better Advisor, Mentor and Friend for my studies. Besides my advisor, I would like to thank the rest of my committee: Dr. N.K. Anand, Dr. Rodolfo Vaghetto, and especially Dr. Thien Nguyen for providing the best experimental data available in literature. I would also like to extend my sincere gratitude to Dr. Elia Merzari, for offering me two invaluable summer internships in his group at Argonne National Laboratory, which allowed me to work on several exciting projects. He is an incredible source of inspiration for my work. (Thanks for all the free lunches). I would like to thank Rosanna Serafini, Alessandro Vanni and Merinda Volia for their precious friendship and help here in Texas. Grazie to my parents, to my brother, grandparents and all the family, to whom this work is dedicated, for the incredible support and love, my role on this earth is to make them proud every single day. Lastly, I would express my gratitude to Meghan, she's the smartest person I know. If you ever read something I wrote, there's 99.9% of chances she corrected the form and most likely also the content of it. The remaining 0.1% is this very short thank you note I wanted to keep in its original form for her, I'm sure she can find a way to make this better too.

CONTRIBUTORS AND FUNDING SOURCES

Contributors

This work was supported by a thesis committee consisting of Dr. Yassin Hassan (advisor), Dr. Rodolfo Vaghetto, Dr. Thien Nguyen of the Department of Nuclear Engineering and Dr. N.K. Anand of the Department of Mechanical Engineering. All work conducted for the thesis was completed by the student, under the advisement of Professor Yassin Hassan of the Department of Nuclear Engineering.

Funding Sources

No additional funding sources were received for this research. All work for the dissertation was completed independently by the student.

TABLE OF CONTENTS

Page

LIST OF FIGURES

Page

LIST OF TABLES

Page

1. INTRODUCTION

A typical commercial pressurized water reactor (PWR) core contains a large number of fuel bundles. Each fuel bundle consists of an array of equally spaced fuel rods. The reference bundle lattice typically consists of a 17×17 square array of equally spaced fuel rods. A single fuel rod has a large length-to-diameter ratio (L/D) with a reference value of 400 (Todreas and Kazimi, 2011).

The reference Reynolds number (Re) for a PWR nuclear reactor core is about 500,000. These factors will induce fluid-elastic instabilities for some of the fuel rods. At such conditions, hydraulic vibrations of the fuel rods, with their axes parallel to the flow, are due to turbulent excitation (Tong and Weisman, 1996). For this reason, spacer grids are required to reduce and withstand such oscillations.

Typical PWR spacer grids are designed with dimples and springs that are in direct contact with the fuel rods, providing the necessary vertical and lateral mechanical support in order to preserve the geometrical configuration of the core during normal and transient scenarios. The presence of spacer grids along the vertical direction of each fuel rod bundle also promotes the mixing rate of the coolant.

In addition, destruction of the fully developed flow symmetry due to the presence of the spacer grids increases the local heat transfer efficiency. In earlier designs of spacer grids, it was found that despite the enhanced heat transfer, local hot spots were present downstream of the spacer grid because of local retardation of the flow over the fuel cladding surface (Tong and Weisman, 1996).

Designs incorporating mixing vanes on the upper edges of the spacer grids have been successful in significantly enhancing the local heat transfer and inter-channel mixing (Tong and Weisman, 1996). In terms of nuclear operating conditions, these design improvements have made it possible to safely increase the power produced by the nuclear reactor core, preventing thermal boiling crises.

The highly turbulent flow structure of the coolant in the region downstream of the spacer grid is particularly challenging to model using traditional computational fluid dynamics (CFD) techniques. High Reynolds number flows present a large spectrum of time and length scales of turbulence. Direct numerical resolution of the Navier-Stokes equations using direct numerical simulation (DNS) techniques is practically impossible due to the limitations of computational resources. For this reason, turbulence modeling plays a key role in reducing the high computational cost.

The majority of turbulent modeling paradigms rely on the ability to model all the turbulence scale. The typical eddy viscosity models are based on the turbulent viscosity hypothesis, which is commonly known as the Boussinesq approximation. The fundamental idea underlying the Boussinesq approximation is to model the turbulence motion in the same way the molecular motion is modeled. However, the molecules and turbulent eddies are inherently different mainly because of the scales they act (Pope, 2000).

The RANS-type models, in particular, tend to model all of the turbulent energy spectrum, which results in a significant compromise between the spatio-temporal resolution and computational cost. In contrast, LES models tend to resolve most of the

energy-containing and inertial scales directly without the modeling burden that is typical of RANS approaches, but with larger computational cost.

A compromise between modeling and computational cost should be found in order to use computational fluid dynamic tools in the most efficient way for this class of problems.

Spacer grids with mixing vanes have received considerable attention among the nuclear engineering community, particularly those involved in CFD simulations. Different benchmark studies have been carried out in the past. The round robin benchmark exercise was carried out against the New Experimental Studies of Thermal-Hydraulics of Rod Bundles (NESTOR) experimental runs for a 5×5 rod bundle with split-type mixing vane grids, considering both isothermal and non-isothermal cases (Kang and Hassan, 2016).
Two types of split vane configurations (swirl-type and split-type) were tested in the Measurement and Analysis of Turbulent Mixing in Subchannels-Horizontal (MATiS-H) test facility benchmark case, the synthesis of the results of the second international CFD benchmark exercise launched by OECD/NEA can be found in (Lee et al., 2014).
The two benchmarks showed an increasing interest, for the nuclear community, for this class of flows.

The main conclusion was the incapability of RANS-based turbulence models of predicting the flow field in the regions where the Reynolds stress anisotropies were predominant. On the other side, scale resolving simulations (mainly LES) models showed a good predicting capability of the flow. In particular in the work of (Bieder et al., 2014) a rational explanation for this general trend of results can be found. Linear turbulent

viscosity models seem to work rather well as long as the cross-flow velocity in the rod gaps is advection controlled (inertial forces predominant), that is directly downstream of the mixing grid. Further downstream, where the cross-flow velocity is reduced and anisotropic turbulence becomes a more and more important mixing phenomena, linear viscosity models can fail.

The following PhD thesis will present results already published and available in the scientific literature, in particular the three main sources will be:

- *Giacomo Busco, Yassin A. Hassan, "Space and energy-based turbulent scale-resolving simulations of flow in a 5 × 5 nuclear reactor core fuel assembly with a spacer grid", International Journal of Heat and Fluid Flow, Volume 71, 2018, Pages 420-441, ISSN 0142-727X, https://doi.org/10.1016/j.ijheatfluidflow.2018.04.003*. (Busco and Hassan, 2018)
- *Giacomo Busco, Elia Merzari, Yassin A. Hassan, "Invariant analysis of the Reynolds stress tensor for a nuclear fuel assembly with spacer grid and split type vanes", International Journal of Heat and Fluid Flow, Volume 77,2019, Pages 144-156, ISSN 0142-727X, https://doi.org/10.1016/j.ijheatfluidflow.2019.04.006*. (Busco et al., 2019)
- *Giacomo Busco, Yassin A. Hassan, "Solution verification of PANS model for a PWR fuel assembly", Nuclear Engineering and Design, Volume 353, 2019, 110213, ISSN 0029-5493, https://doi.org/10.1016/j.nucengdes.2019.110213*. (Busco and Hassan, 2019)

2. OBJECTIVE OF THE THESIS

We have addressed two key important aspect for the modeling and simulation of the turbulent flow across a nuclear reactor spacer grid: (1) the turbulence modeling vs. computational resources and (2) the importance of the correct prediction of the Reynolds stress anisotropy tensor. In the study we will focus our attention to both of the key points listed above.

The first objective will be to find a compromise between turbulence resolution and computational cost for validation purposes. The finite volume commercial code STAR-CCM+ will be used to perform the analysis. We will present the theoretical aspects and practical applications of the PANS turbulence model. An energy-based variable resolution (VR) model that can span from RANS-like solution to DNS-like solution without changing the form of the closure model. We will be able to control the ratio *turbulence modeling burden to computational cost* by adjusting the energy-based PANS filter applied to the Navier-Stokes equations. The filter controls the ratio of resolved turbulent scales to the modeled turbulent scales. A V&V methodology for this model will be presented. We validated the simulations results using the available experimental data (Nguyen and Hassan, 2017). Their stereoscopic PIV measurements provides the three-components of the velocity fields and their associated statistical results. We consider these data are the most appropriate configuration, i.e. in terms of geometries and studied Reynolds numbers, for our numerical simulations.

The second objective will be to show and analyze the importance of the correct prediction of the Reynolds stress tensor anisotropies for this class of flow. The analysis will be performed with the high-order spectral elements methods technique for the discretization of the Navier-Stokes equations. The open source Nek5000 code developed at Argonne National Laboratory (ANL) will be used for the second part of the analysis. The focus will be on the study of the turbulent flow structure described by the turbulent anisotropy invariant analysis of the Reynolds stress tensor. The Lumley's anisotropy invariant mapping will be used as main investigation technique to better analyze the physics associated with this class of flows, as previously done, for example, by (Merzari and Ninokata, 2011) for the infinite bare rod bundle case.

First and second order statistics of the flow field will be validated by a code-to-code comparison from the PANS/LES results and experimental stereoscopic PIV results of (Nguyen and Hassan, 2017). The study will contribute to an invaluable resource to further refine RANS turbulence models and deepen the understanding of the flow physics in this class of flows.

3. TURBULENCE AND NUMERICAL MODELING

The Navier-Stokes equations represent the best mathematical model available for incompressible fluid flows. However, it is known that direct numerical resolution of the Navier-Stokes equations imposes significant computational resources and therefore, turbulence modeling plays an important role to overcome this drawback.

The Navier-Stokes equations for mass and momentum transport of incompressible flows are given by:

$$\frac{\partial u_i}{\partial x_i} = 0 \tag{1}$$

$$\frac{\partial u_i}{\partial t} + u_j \frac{\partial u_i}{\partial x_j} = -\frac{1}{\rho}\frac{\partial p}{\partial x_i} + \nu \frac{\partial^2 u_i}{\partial x_j \partial x_j} \tag{2}$$

Various turbulence models have been proposed and widely studied in the literature. The computational extent of these models is directly proportional to the desired degree of resolution of the flow. The two extremes of turbulence modeling for engineering applications are represented by the RANS and LES models.

The typical two-equation RANS models are based on the eddy viscosity hypothesis, which is commonly known as the Boussinesq approximation (Pope, 2000). The fundamental idea underlying the Boussinesq approximation is to model the turbulence motion in the same way the molecular motion is modeled. However, the molecules and

turbulent eddies are inherently different mainly because of the scales they act (Pope, 2000). The Boussinesq approximation is based on the assumption that there is a linear relation between the deviatoric part of the Reynolds stress tensor $\tau_{ij}^{Re} = -\rho\,\overline{u_i' u_j'}$, which is the modeled part of the flow, and the mean strain rate tensor $S_{ij} = \frac{1}{2}\left(\frac{\partial \overline{u_i}}{\partial \overline{x_j}} + \frac{\partial \overline{u_j}}{\partial \overline{x_i}}\right)$, which is the resolved part of the flow:

$$-\rho\,\overline{u_i' u'_j} = 2\,\mu_t\,S_{ij} \tag{3}$$

The main drawback of the Boussinesq approximation is that the turbulent viscosity μ_t merely acts as a constant of proportionality between the two deviatoric parts of such tensors, causing each stress component τ_{ij} to act with the same extent and intensity for each of the corresponding strain rates S_{ij}. The consequence of such a hypothesis is that the anisotropy effects cannot be captured. This is why various RANS models fail in capturing the flow physics of mixing vanes, where strong secondary flow structures arise and develop in the region downstream of the spacer grid. In RANS modeling, the introduction of the turbulent viscosity itself ensures that all of the turbulent scales are completely modeled and all types of flow instabilities will be dumped. Hence, only the mean flow quantities of interest are retained.

The use of space filtering operators enables one to resolve all of the turbulent scales that are larger than the grid size. In LES, the filter width is closely related to the grid size. The larger the cut-off wave number, the more accurate the computation will be because

more scales are resolved and only the smallest scales are modeled. The main outcome of the filtering operation is that the modeled eddy viscosity ν_t of the flow is reduced, giving more freedom for the flow to develop naturally under the action of inertial, non-linear, induced instabilities. However, the LES closure assumptions are completely invalid if the cut-off wave number is within the energy-containing scales or large inertial scales and therefore, more detailed characterization of the unresolved scales is needed at such a cut-off wave number (Girimaji, 2006).

PANS models belong to a class of bridging models where the closure model has the natural tendency to resolve the turbulent scales by changing the implicit filter control parameters. Two types of PANS filters have been identified: the unresolved-to-total kinetic energy ratio f_k and the unresolved-to-total dissipation rate ratio f_ϵ.

Fixed-point analysis, which is commonly used to understand the asymptotic behavior of turbulent flows, has shown that PANS models have the natural ability to reduce the eddy viscosity ν_t during the course of the simulations (Lakshmipathy and Girimaji, 2006), unlike unsteady RANS (URANS) simulations, which tend to produce excessive energetic unresolved scales of motion such that the eddy viscosity of the unresolved scales attain non-physical large values, resulting in a quasi-steady RANS-type solution. This is also demonstrated in this work.

An arbitrary generalized filter operator $<\cdot>$ is applied to the Navier-Stokes equations in order to decompose the instantaneous velocity field V_i into the resolved (filtered) $U_i = < V_i >$ and unresolved (unfiltered) u_i parts such that: $V_i = U_i + u_i$ and $U_i = < V_i >$, with $< u_i > \neq 0$ (Girimaji, 2006).

The momentum equation is reduced to its partially filtered representation:

$$\frac{\partial U_i}{\partial t} + U_j \frac{\partial U_i}{\partial x_j} + \frac{\partial \tau(V_i, V_j)}{\partial x_j} = -\frac{1}{\rho}\frac{\partial < p >}{\partial x_i} + \nu \frac{\partial^2 U_i}{\partial x_j \partial x_j} \tag{4}$$

Filtering the non-linear advection term in the Navier-Stokes equation gives rise to the generalized central second moment: $\tau(V_i, V_j) = < V_i V_j > - < V_i >< V_j >$. Introducing the definition of the generalized central moment makes the filtered equations independent of the filter being adopted and this approach is formally equal to the classical RANS approach. This property was introduced by (Germano, 1992) under the name "averaging-invariance". It is one of the most important properties used in PANS theory to develop the bridging features between RANS modeling and DNS.

As discussed in detail in Girimaji (2006), the PANS modeling approach is different from LES in three key aspects: (1) the velocity field is decomposed based on the turbulent kinetic energy content rather than the cut-off wave number as in many LES approaches, (2) the filter demarcating the resolved and unresolved parts of the velocity is implied in PANS modeling and therefore, there are no filtering operations involved during the computations, (3) the closure relation (subfilter scale) is independent of the domain discretization (grid size). We will discuss the PANS and LES closure modeling based on the application of an arbitrary generalized filter operator as well as the averaging-invariance principle.

3.1. LES closure modeling

We selected the wall-adapting local eddy viscosity (WALE) subgrid stress closure model in this study (Nicoud and Ducros, 1999). This model is based on the square of the velocity gradient tensors, accounting for the effect of the strain tensor S_{ij} and rotation rate tensor Ω_{ij} of the smallest turbulent fluctuations. The closure of the eddy viscosity is expressed in algebraic form as in many LES closures:

$$v_t = (C_w \Delta)^2 \frac{(S_{ij}^d S_{ij}^d)^{\frac{3}{2}}}{\left(\overline{S_{\imath\jmath}}\,\overline{S_{\imath\jmath}}\right)^{\frac{5}{2}} + (S_{ij}^d S_{ij}^d)^{\frac{5}{4}}} \tag{5}$$

$$S_{ij}^d = \overline{S_{\imath k}}\,\overline{S_{\imath k}} + \overline{\Omega_{\imath k}}\,\overline{\Omega_{\imath k}} - \frac{1}{3}\delta_{ij}(\overline{S_{mn}}\,\overline{S_{mn}} - \overline{\Omega_{mn}}\,\overline{\Omega_{mn}}) \tag{6}$$

It shall be noted that the closure relation takes into account the rotational part of the velocity tensor gradient, which provides physical insight into the flow where secondary flow is the dominant part of the problem. Explicit filtering is not required in building the eddy viscosity model, contrary to other LES methods, since only the filtered local flow quantities are needed. The wall behavior is better modeled by proper scaling of the eddy viscosity close to the wall compared to the Smagorinsky model (Nicoud and Ducros, 1999).

3.2. PANS Closure Modeling

RANS models are purported for averaging all turbulent scales of motion and hence, these models carry sufficient physics to accurately represent the averaged fields (Girimaji, 2006). The idea of RANS modeling is that, since all of the turbulent scales are eliminated, the various effects of the eliminated scales must be modeled. Based on our experience in RANS modeling, it is necessary to acquire knowledge of the kinetic energy k_u and dissipation ϵ_u of the unresolved scales for the PANS equations. Hence, in the PANS bridging turbulent modeling paradigm, it is only natural to use turbulent kinetic energy and dissipation to define the filters. The unresolved-to-total kinetic energy ratio f_k and unresolved-to-total dissipation ratio f_ϵ are used to express the degree of turbulent flow resolution or the extent to which we want to model the unresolved part of the flow:

$$f_k = \frac{k_u}{k}, f_\epsilon = \frac{\epsilon_u}{\epsilon} \tag{7}$$

The PANS *k*-ω model (Lakshmipathy and Girimaji, 2006) is used in this work based on the cut-off parameters presented above. Thus, the evolutionary equations for the unresolved turbulent kinetic energy k_u and the specific dissipation rate ω_u are given by:

$$\frac{\partial k_u}{\partial t} + U_j \frac{\partial k_u}{\partial x_j} = P_u - \beta^* k_u \omega_u + \frac{\partial}{\partial x_j}\left[\left(\nu + \frac{\nu_u}{\sigma_{ku}}\right)\frac{\partial k_u}{\partial x_j}\right] \tag{8}$$

$$\frac{\partial \omega_u}{\partial t} + U_j \frac{\partial \omega_u}{\partial x_j} = \alpha \frac{\omega_u}{K_u} P_u - \beta' \omega_u^2 + \frac{\partial}{\partial x_j}\left[\left(\nu + \frac{\nu_u}{\sigma_{\omega u}}\right)\frac{\partial \omega_u}{\partial x_j}\right] \tag{9}$$

The modified closure coefficients derived from fixed-point analysis are defined as:

$$\beta' = \alpha\beta^* - \alpha\frac{\beta^*}{f_\omega} + \frac{\beta}{f_\omega} \tag{10}$$

$$\sigma_{ku} = \sigma_k \frac{f_k}{f_\omega} \tag{11}$$

$$\sigma_{\omega u} = \sigma_\omega \frac{f_k}{f_\omega} \tag{12}$$

where $f_\omega = \omega_u/\omega$ can be expressed in terms of f_k and f_ϵ as follows, noting that $\omega = \beta^* k\epsilon$:

$$f_\omega = \frac{f_\epsilon}{f_k} \tag{13}$$

The standard Wilcox *k-ω* closure coefficients are $\alpha = 5/9$, $\beta^* = 0.09$, $\beta = 0.075$, $\sigma_\omega = 0.5$, and $\sigma_k = 0.5$. The two-equation PANS closure model has the same form of the

parent RANS equation, which is expressed in terms of the unresolved kinetic energy and dissipation:

$$\nu_u = C_\mu \frac{k_u^2}{\epsilon_u} = \frac{k_u}{\omega_u} \tag{14}$$

The f_ϵ parameter is usually set equal to one (i.e., $f_\epsilon = 1$) when the intended cut-off filter is used within the inertial range and the dissipative scales do not need to be resolved.

3.3. Spectral Element Method

In the second part of the present study we used the open-source code Nek5000. It is based on the spectral element method (Patera, 1984). It uses high-order weighted residual technique that combines the geometric flexibility of finite elements with the rapid convergence and tensor-product efficiencies of global spectral methods. Higher order methods allow for more accurate solutions that minimize numerical dispersion and dissipation (Deville et al., 2002). The domain is spatially discretized with smaller hexahedra subdomains (elements) that conforms to the domain boundaries (Merzari et al., 2016). Within each element the velocity-pressure space is typically a space of *N-th* order Lagrange polynomial interpolant, based on tensor-product arrays of *N+1* Gauss-Lobatto-Legendre (GLL) collocation points. The result is a pressure velocity coupled system of equations: three Helmotz equations for velocity and one Poisson equation for pressure. In

the present we performed two simulations by increasing the local order of the polynomial interpolant from *N = 6 to N = 8* in order to test the numerical convergence of the first and second order statistics. In the absence of eddy viscosity, some type of numerical stabilization is required (Fischer and Mullen, 2001). A filtered-based stabilization is employed because of numerical instabilities that can arise for moderate and high Reynolds number, due to the accumulation of numerical errors similar to aliasing errors in pseudo-spectral methods (Ohlsson et al., 2011). An explicit low-pass filter is applied at the end of each time step to suppress high wavenumber instabilities. In the present study the last two coefficients corresponding to the *(N-1)-th* and *N-th* order Lagrange interpolants are reduced in magnitude by the application of a low-pass filter. Its transfer function is a parabola, whose value corresponding to the *N-th* order is $\alpha = 0.05$. Temporal discretization is based on high-order splitting that is third-order accurate in time and reduces the coupled velocity-pressure problem to four independent elliptic solves per time step: one for each velocity components and one for the pressure. A characteristics-based time-stepping (Maday et al., 1990) has been used to avoid the limitations imposed by the Courant–Friedrichs–Lewy (CFL) number due to the explicit treatment of the non-linear convection term. An average maximum CFL of 1.5 has been reached during the simulation of the numerical transient.

4. GEOMETRY AND SPATIAL DISCRETIZATION

The test case is a scaled PWR fuel rod bundle with a 5×5 lattice. Figure 1 shows some of the geometrical details of the computational domain. All of the dimensions such as the bundle pitch (12.6 mm), rod diameter (9.5 mm), and spacer grid features (dimples, springs, and mixing vanes) are identical to the full scale 17×17 lattice fuel rod bundle. The value used for the hydraulic diameter was $D_h = 10\ mm$. The only difference is the 5×5 lattice arrangement versus the 17×17 lattice arrangement.

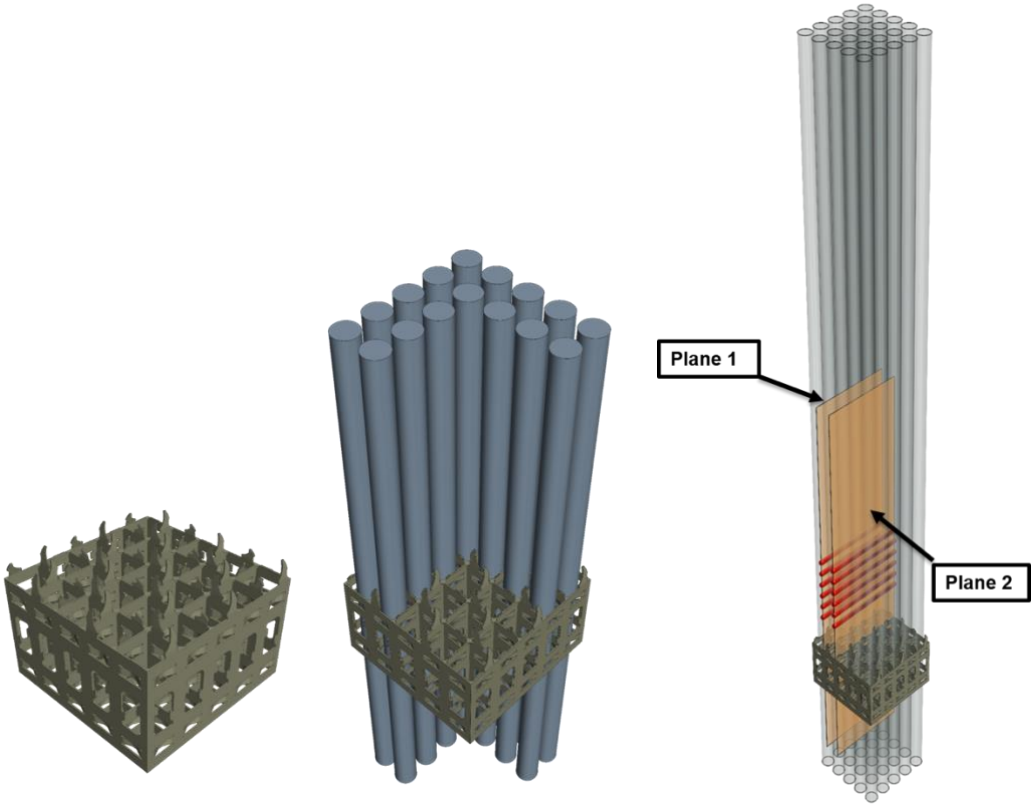

Figure 1 Spacer grid geometry features. Reprinted from Busco et. al, 2018.

4.1. STAR-CCM+ Mesh

An unstructured trimmed mesh was created due to the highly complex geometry of the fuel rod bundle with dimples, springs, and mixing vanes. The hexahedral mesh structure was kept as homogeneous as possible in order to ensure that most of the computational domain was covered with a predominant structured-like mesh. Large spatial resolution was imposed in the mixing vane region in order to generate a good quality mesh. The volume change, cell quality, skewness angles, and aspect ratios were evaluated to ensure quality of the discretized computational domain. The wall regions were discretized using 14 and 2 prism layers in the bundle region and spacer grid region, respectively.

We observed that a large number of parallel prismatic layers in the spacer grid region adversely affects the mesh quality. In fact, this will cause the formation of large cells boundary skewness angles. The skewness is a measure that reflect whether the cells on either side of a face are formed in such a way as to permit diffusion of quantities between cells centroids. Large skewness angles (above 90°) were present in the spacer grid region. This factor was compromising the convergence of the numerical scheme. Local large residuals were present in this region, due to the large skewness of some prismatic layer cells. The reduction to 2 prismatic layers solved the issue.

Two computational meshes were tested, where a coarse mesh with 25 million cells was used mainly for the PANS models. For this mesh, we imposed a refined spacer grid region with a homogeneous grid size of $0.02\,D_h$ and $0.04\,D_h$ in the core and bundle

region, respectively. We adopted a finer mesh with 100 million cells for the LES model with a homogeneous grid size of $0.02\ D_h$ throughout the domain. Figure 2 shows some mesh details.

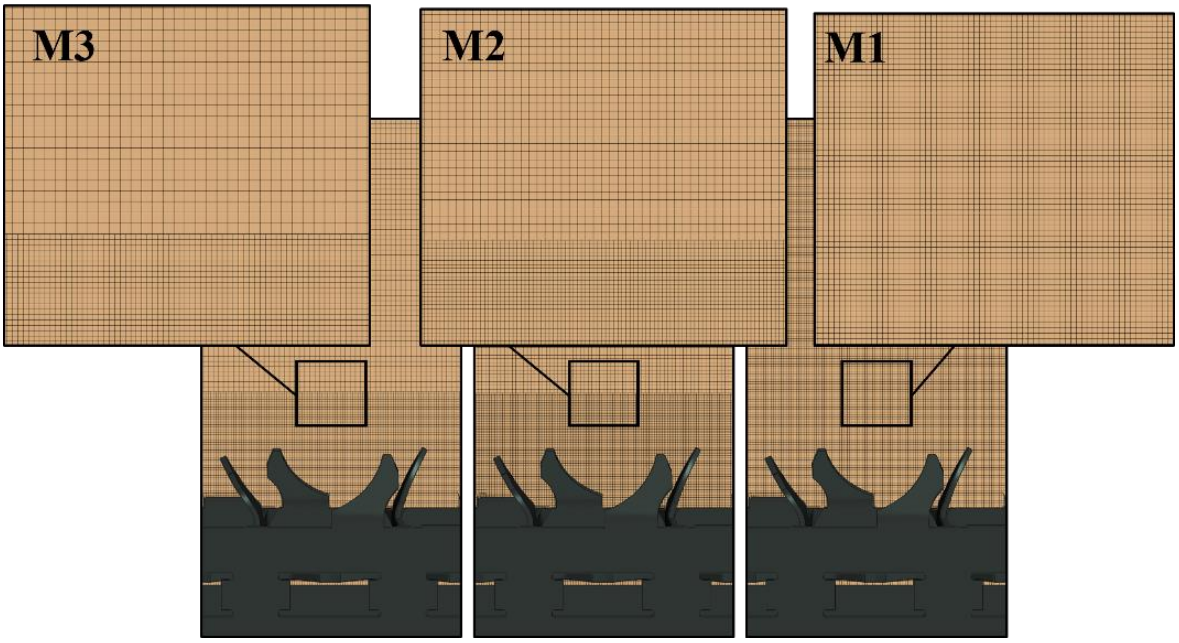

Figure 2 STAR-CCM+ trimmed mesh details. M1 fine mesh. M2 medium mesh. M3 fine mesh. Reprinted from Busco et. al, 2018.

The overall average y^+ value was less than one for both PANS and LES models. The surface mesh size in the axial direction and azimuthal direction in the bundle region was less than 10, in non-dimensional wall units, for PANS simulations, and less than 5 for the LES simulation.

The all-y+ wall treatment was used. The all-y+ wall treatment is a hybrid wall treatment that attempts to combine the high y+ wall treatment for coarse meshes and the low y+ wall treatment for fine meshes. It is designed to give results similar to the low-y+

treatment as y+ < 1 and to the high-y+ treatment for y+ > 30. The all-y+ method blends turbulence quantities such as dissipation, production, stress tensor, etc. calculated by the high-y+ approach or by the low-y+ approach using an exponential weighing function (STAR-CCM+, 2015).

In addition, we performed mesh sensitivity study for the PANS models, since PANS closure modeling is decoupled from the grid being used. It is worth noting that mesh sensitivity study should always be performed to check the convergence of the models, as in RANS simulations.

In order to obtain a good estimation of the best grid size for a given PANS filter (f_k, f_ϵ), based on Kolmogorov's scaling theory (Reyes et al., 2014), it has been demonstrated that the corresponding cut-off scale Δ_c can be estimated as:

$$\Delta_c \sim C_\mu^{\frac{3}{2}} \frac{f_k^{\frac{3}{2}}}{f_\epsilon} L \tag{15}$$

where $L = k^{3/2}/\epsilon$ is the estimated turbulent integral length scale. Hence, the computational grid size Δ should be smaller than the evaluated cut-off length scale (i.e., $\Delta_c > \Delta$).

We conducted a priori estimation of these scales by precursor runs using the steady-state RANS *k*-ω model. Based on the scaling arguments, we found that our mesh for PANS modeling fulfils the criterion above for up to $f_k = 0.4$.

4.2. Nek5000 Mesh

Nek5000 only supports hexahedral mesh elements. Due to the very complex geometrical structure of the spacer grid, the generation of a structured mesh is very challenging. To overcome those difficulties a *tet-to-hex* strategy has been adopted. The strategy consists in creating a tetrahedral mesh for the spacer grid region first. Then the mesh is converted to hexahedra. Figure 3 represents the mesh generation and conversion steps.

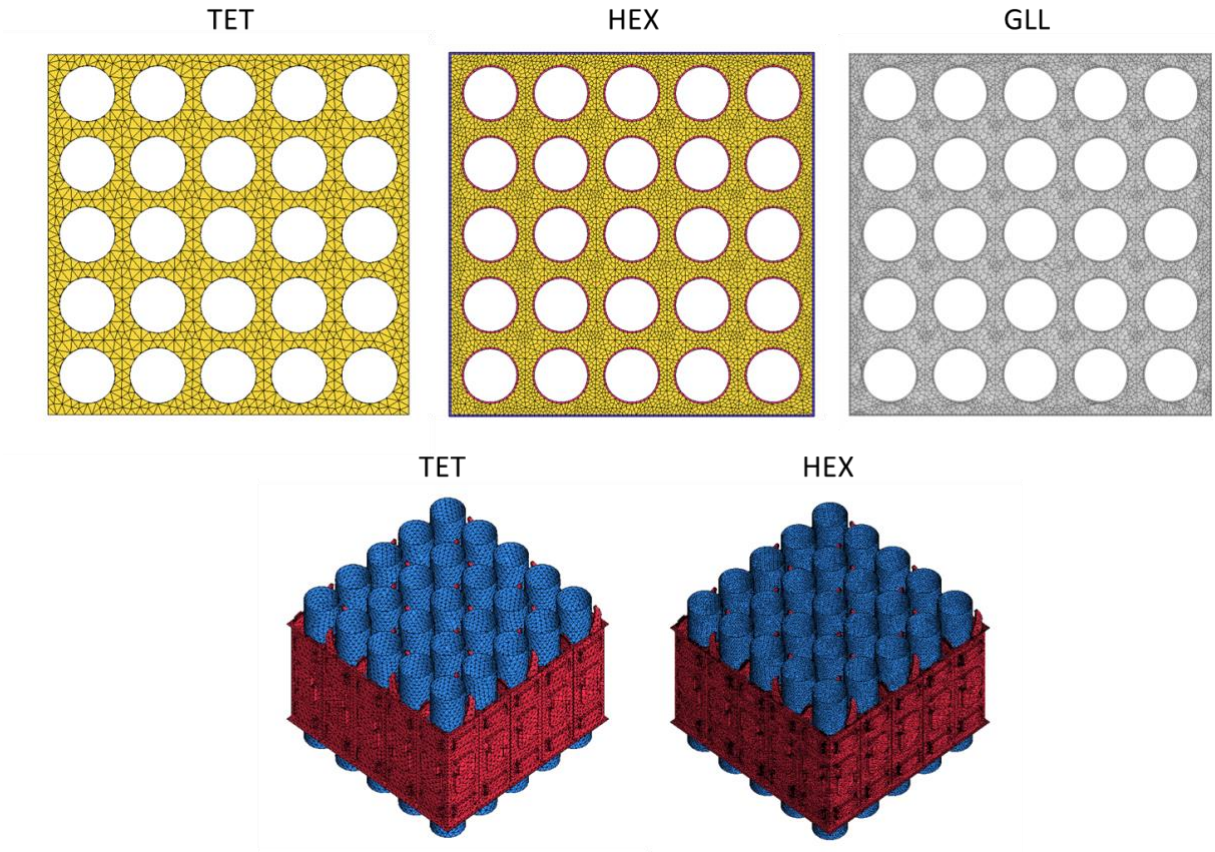

Figure 2 TOP: mesh conversion: Tetrahedral (left), Hexahedral (center), GLL integration points (right). BOTTOM: spacer grid meshing before extrusion.

The conversion is such that each tetrahedron is subdivided into three different hexahedra. In order to better resolve the wall region an extrusion of the mesh normal to the wall surface has been performed. The extruded prismatic layer is visible in figure 3.

The next step was to create mid-sides nodes on the elements faces (hex-20) and project the extruded prism layer to the wall to better capture the geometrical features such as rods wall curvatures. The final step was to extrude in the upstream and downstream region the upper and lower surfaces of the spacer grid region.

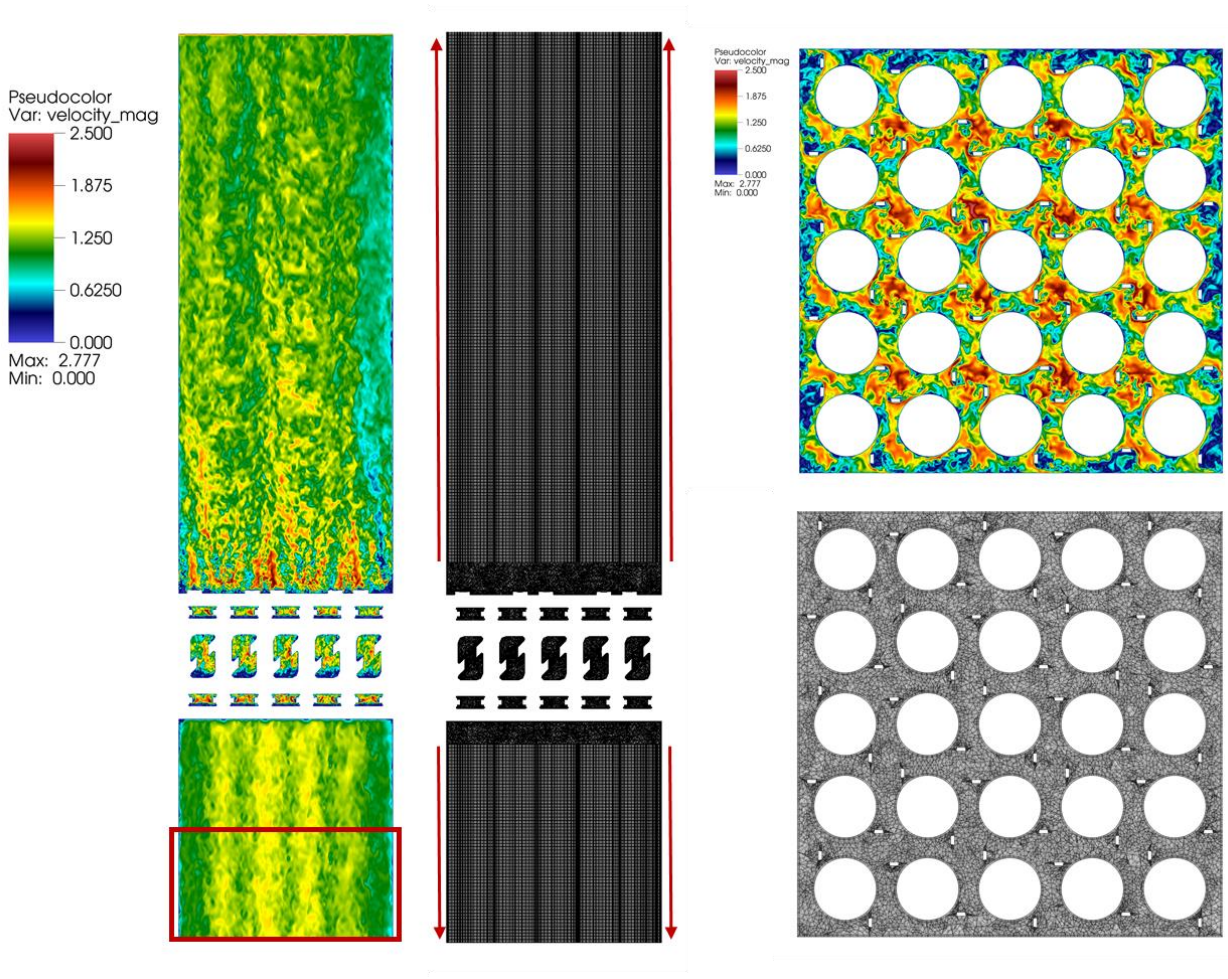

Figure 3 Recirculation inlet region (red box). Mesh extrusion (red arrows).

In Figure 4 the mesh extrusion from the spacer grid region is presented. The final element count for the computational domain was 4 millions of hexahedral elements. The generation of the tetrahedral mesh was performed by ANSYS-MESH and the conversion to hexahedral structure was performed with ANSYS-ICEM.

In order to be able to have a fully developed inlet flow condition, a recirculation region before the spacer grid has been implemented. The region extends for 4 hydraulic diameters, the spacer grid has been placed 5 hydraulic diameters downstream the recirculation region. The recirculation region extension of $4\ D_h$ has been judged sufficient, a two points correlation study in the downstream region of the grid spacer will show that the maximum extent of the two-point correlation profile was less than $1\ D_h$ and the maximum integral length scale less than $0.5\ D_h$. The domain then extends up to 16 hydraulic diameters downstream the vane region (y-direction).

In Figure 4 the inlet recirculation region is highlighted. Since a full recovery of the fully develop flow is not reached at the end of the computational domain ($y/Dh=16$), whenever we will address the turbulent structure in the fully developed region ($y/Dh = \infty$) we will present results from the recirculation inlet region.

5. METHODOLOGY: MATHEMATICAL TOOLS AND NUMERICAL ANALYSES

5.1. PANS simulations setup

The Reynolds number used in our simulations is $\mathrm{Re} = 14{,}000$, which is based on the hydraulic diameter D_h. The selected Reynolds number has been selected in order to co-validate the (Nguyen and Hassan, 2017) experimental data. The average velocity in the bundle (based on the Reynolds number) was used as the normalization factor, $V_0 = 1.33\ \mathrm{m/s}$. The transient simulations were run until a statistically steady-state turbulent condition was achieved. All of the turbulence statistics were collected starting from this condition. Four PANS simulations were performed based on four different cut-off parameters.

	URANS	CASE 1	CASE 2	CASE 3	LES
f_k	1	0.8	0.6	0.4	0.1
f_ϵ	1	1	1	1	—
f_ω	1	1.25	1.66	2.5	—

Table 1 PANS filters adopted in the study

During the post-processing phase, we found that the equivalent unresolved-to-total kinetic energy ratio f_k for LES is $f_k = 0.1$, which means that ~90% of the turbulent energy has been directly resolved.

During the course of the simulations, we observed that the spatio-temporal discretization significantly affects the performance of the PANS models. It is known that low-order spatio-temporal discretization tends to generate large amounts of numerical dissipation, which will damp all types of flow instabilities and the solution decays to a RANS-like solution.

Thus, we adopted second-order temporal discretization and third-order spatial discretization schemes (i.e., third-order hybrid Monotonic Upwind Scheme for Conservation Laws (MUSCL)) in this study.

For the LES model, we adopted a second-order temporal discretization scheme and a bounded central-differencing scheme for spatial discretization in order to maintain the robustness of the numerical scheme.

We obtained the inlet boundary conditions for all cases by performing precursor simulations of the upstream region of the bundle using the LES model. Periodic boundary conditions were imposed in order to obtain a fully developed turbulent flow. We used the synthetic eddy method to initialize the turbulence in the bare bundle domain.

5.2. PANS Solution verification and model validation

The PANS model closure relation is independent from the grid size. The filtering process is based on the turbulent kinetic energy content of both resolved and unresolved flow field. To validate the numerical solution of the PANS models two main activities

were performed: mesh sensitivity analysis and the application of an internal consistency criterion.

The mesh sensitivity study has been carried for two main reasons: to ensure that the imposed PANS filter was commensurate with the give spatial discretization, and to have an estimate of the numerical discretization error using the grid convergence index (GCI) analysis. When a given PANS filter is imposed, a posteriori consistency analysis must be performed to ensure that the externally imposed filter, which is the ratio of the unresolved-to-total turbulent kinetic energy of the flow, has been maintained throughout all the course of the simulation.

As reported in (Mahaffy et al., 2015) three main sources of numerical error for a CFD simulation are: round-off error, iteration error and numerical discretization error.

The first two type of errors have been controlled by using double-digits precision and attaining residuals levels, in all the domain and for each time step, low enough to be considered negligible in the present study.

In addition, the collection of time statistics of key quantities like time averaged velocity and its variance at different key points was monitored, and it reached a good degree of time invariant convergence.

The discretization error for a converged solution, is the main source of the numerical error part, and the most difficult to evaluate. For the estimation of its magnitude we have used the Roache's GCI method (Roache, 1997).

For a given quantity of interest Φ, the GCI is defined as:

$$GCI = \frac{F_s}{r^p - 1}\left|\frac{\phi_2 - \phi_1}{\phi_1}\right| \tag{16}$$

where r is the ratio of two refined mesh sizes (a refinement ratio of 1.3 has been used for this case), Φ_i is the target value measured on the i-th refined mesh (1 indicates the finest mesh, 3 indicates the coarsest mesh), $F_s = 3$ a safety factor and p, is the observed order of accuracy defined as:

$$\mathrm{p}_{obs} = \frac{\ln\left[\frac{\phi_3 - \phi_2}{\phi_2 - \phi_1}\right]}{\ln(r)} \tag{17}$$

The latter has been evaluated to quantify the degree of mesh convergence for the numerical solution.

The PANS filter f_k represents the ratio between the unresolved and total turbulent kinetic energy of the flow. When such a filter is imposed, an internal consistency check should be performed to evaluate the validity of the closure model.

Unlike the LES closure model, the PANS closure model is not directly coupled to the resolution of the discretized domain. In order to validate the effectiveness of the imposed filter, it is necessary to verify if the actual partition between the resolved and unresolved fields has been achieved during the course of the simulations (Razi et al., 2017).

The most appropriate internal consistency test involves evaluating the imposed-to-computed eddy viscosity, because the eddy viscosity plays an important role in the governing equations as a result of global filtering and it is the actual bridging parameter between the filtered and unfiltered domains.

In order to confirm the aforementioned statement, we evaluated the ratio of the PANS turbulent viscosity $\nu_{u,t}$ to the RANS turbulent viscosity ν_t.

The PANS turbulent viscosity is defined as:

$$\nu_{u,t} = C_\mu \frac{k_u^2}{\epsilon_u} = \frac{k_u}{\omega_u} \tag{18}$$

where the subscript *u* indicates the unresolved (unfiltered) component of the flow field.

The RANS turbulent viscosity is defined as:

$$\nu_t = C_\mu \frac{k^2}{\epsilon} = \frac{k}{\omega} \tag{19}$$

where due to the RANS paradigm, the turbulent quantities are supposed to be the total modeled component of the unresolved field.

The ratio of these turbulent viscosities, called the recovery ratio (Lakshmipathy, 2009), can be recast in the following form:

$$f_\nu = \frac{\nu_{u,t}}{\nu_t} = \frac{f_k^2}{f_\epsilon} \tag{20}$$

where $f_k = k_u/k$ and $f_\epsilon = \epsilon_u/\epsilon$.

We imposed the dissipation filter to be $f_\epsilon = 1$ and thus, the recovery ratio becomes $f_\nu = f_k^2$.

The three PANS filters ($f_k = 0.8$, $f_k = 0.6$, and $f_k = 0.4$) result in a recovery ratio of $f_\nu = 0.64$, $f_\nu = 0.36$, and $f_\nu = 0.16$, respectively, which will be used for the internal consistency test.

We evaluated the distribution of the recovery ratios for our simulations on Plane 1 and Plane 2 (Figure 1) in the region downstream of the spacer grid, regions selected because of interest for validation with experiments purposes.

To better represent the results, and compare them with the experiments, a validation metrics have been introduced. We evaluated the relative error between the experimental data and our CFD turbulent models numerical results as:

$$Error[\%] = \frac{1}{N} \sum_{i=1,N} \left| \frac{Exp_i - CFD_i}{Exp_i} \right| \tag{21}$$

Where *i* is the measurement location of the experimental data and N is the total number of points. CFD simulation results have been interpolated by using cubic splines at the same locations as PIV measurements points. Two quantities have been monitored for both experiments and numerical simulations: the mean flow kinetic energy (MKE) and

total turbulent kinetic energy profiles (TKE) at different locations downstream the spacer grid. We used such data since the velocity and RMS components, especially in the horizontal directions, were very close to zero, giving very large values relative errors. Nonetheless the evaluation of a validation metrics based on the energy of the flow, offered the opportunity to have a global representation of the validation results.

5.3. PANS spatio-temporal analysis tools

PANS model has a natural tendency to produce results similar to those for LES when the filters magnitudes are small. The PANS models with the larger filters tend to resolve the largest turbulent scales.

By using a different set of PANS filters, we can place the energy-based cut-off filter f_k at different intervals within the turbulent kinetic energy spectrum. Larger PANS filters will enable us to resolve only the largest turbulent scales in the computational domain in both space and time.

5.3.1. Temporal analysis

We will perform the temporal analysis of the resolved turbulent flow structure for the PANS and LES models by applying a time autocorrelation operator in order to evaluate the resolved turbulent time scales.

The normalized autocorrelation operator is defined as:

$$T_{ii}(x_p, \tau) = \frac{\langle V_i^{'}(x_p, t)\, V_i^{'}(x_p, t+\tau)\rangle}{\langle V_i^{'\,2}(x_p, t)\rangle} \tag{22}$$

where x_p is the space point within the computational domain wherein the fluctuating velocity components are analyzed and τ is the time lag between two time points.

We evaluated the fluctuating velocity components $V_i^{'}$ at four locations downstream of the spacer grid. The fluctuating velocity components $V_i^{'}$ were assessed along the vertical line at the center of one of the subchannels adjacent to the central rod, as shown in Figure 5.

The integral time scales were estimated using the following equation:

$$T_{int}^{ii} = \int_0^{\tau^*} T_{ii}(x_p, \tau) d\tau \tag{23}$$

where the upper integral limit τ^* is taken as the value where the autocorrelation $T_{ii}(x_p, \tau)$ reaches zero.

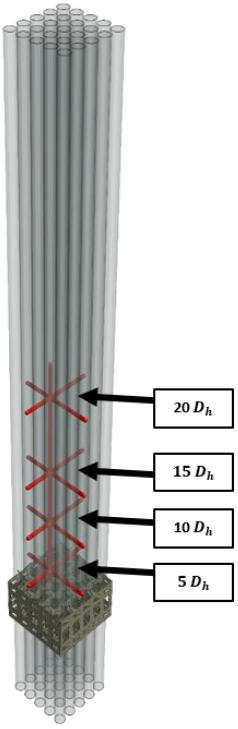

Figure 4 Locations of the probes downstream of the spacer grid for spatio-temporal analysis of the fluctuating velocity components.

5.3.2. Spatial analysis

In order to test the modeling capability of the PANS models, we performed a two-point correlation analysis of the time signals for the fluctuating velocity components $V_i^{'}$.

It shall be noted that the spatial analysis was performed at the same locations along the fuel rod bundle configuration as those for the temporal analysis.

The normalized two-point correlation is defined as:

$$R_{ii}(x_p, \eta) = \frac{\langle V_i^{'}(x_p)\, V_i^{'}(x_p + \eta)\rangle}{\sqrt{\langle V_i^{'}(x_p)\rangle}\sqrt{\langle V_i^{'}(x_p + \eta)\rangle}} \tag{24}$$

The integral length scale, analogous to the integral time scale, can be defined as:

$$L_{int}^{ii}(x_p) = \int_0^{\eta^*} R_{ii}(x_p, \eta)\, d\eta \tag{25}$$

where, as before, the integration upper limit η^* is taken as the value where the two-point correlation is zero.

5.4. Representation of the Turbulent Anisotropic State

Invariant analysis of the Reynolds stress tensor anisotropy can give an accurate and deep intuitive understanding of the turbulent structure of a turbulent flow. Lumley's triangle has proven to be a powerful representation of the invariant analysis of the second-order statistics collection provided by the Reynolds stress tensor. Any realizable Reynolds stress that can occur in a turbulent flow correspond to a point in the Lumley triangle (Lumley and Newman, 1977). It is interesting to study the Reynolds stress anisotropic tensor for different reasons. In the turbulent viscosity modelling approach, the main

assumption is that the anisotropic stress tensor D_{ij} is aligned with the strain rate tensor S_{ij} (Pope, 2000).

For such modeling approach it is the deviatoric part of the Reynolds stress tensor effecting on the transportation mechanism of momentum. In a typical RANS two-equations eddy-viscosity model the five independent components of such tensors are related to each other by the eddy viscosity constant ν_t, meaning that each component of D_{ij} acts with the same strength and intensity on each corresponding component of S_{ij}, without any directional dependence.

It is also well known that secondary flows structures can results from a nonzero difference in the normal Reynolds stresses on the plane normal to the flow direction. Different eddy viscosity turbulence models don't have a natural mechanism for the development of secondary flow (Speziale, 1982). Prediction of the amount and type of anisotropy, the return-to-isotropy behavior responsible for the exchange of turbulent kinetic energy among its components through the interaction of fluctuating velocities and pressure, has found in the Lumley's triangle representation and invariant analysis a meaningful tool for the development of first and second-order modelling of turbulent flows (CHOI and LUMLEY, 2001). As a symmetric positive semi-definite second order tensor, the Reynolds stress tensor R_{ij} can be decomposed in an isotropic part I_{ij} and a deviatoric (anisotropic) part D_{ij}:

$$R_{ij} = I_{ij} + D_{ij} \tag{26}$$

$$I_{ij} = \frac{1}{3} R_{ip}\delta_{pj} = \frac{2}{3} k\delta_{ij} \tag{27}$$

$$D_{ij} = R_{ij} - I_{ij} \tag{28}$$

The normalized anisotropic tensor is defined by:

$$B_{ij} = \frac{D_{ij}}{2k} \tag{28}$$

The three invariants of the normalized anisotropic tensor can be found by solving the Cayley-Hamilton equation:

$$\det\left(B_{ij} - \sigma\delta_{ij}\right) = 0 \quad \leftrightarrow \quad \sigma^3 - I\sigma^2 + II\sigma - III = 0 \tag{29}$$

Where the three invariants associated with the matrix are:

$$I = trace(B) \tag{30}$$

$$II = \frac{1}{2}\{[trace(B)]^2 - [trace(B^2)]\} \tag{31}$$

$$III = \det(B) \tag{32}$$

The characteristic equation associated with the matrix also provides three eigenvalues and three eigenvectors of the turbulence anisotropic tensor. The normalized anisotropic tensor *B* has zero trace. By taking advantage of such property it is possible to represent it by the main two non-zero invariants *II* and *III*, instead of its five independent components.

The Lumley triangle is the map that represent the invariant states of the tensor *B* for each point of the physical space. The borders of the domain represent the realizable limits of the turbulent stress tensor. We will use the η, ξ coordinates (Choi and Lumley, 2001) to better represent the non-linearities in the turbulent return to isotropy trajectories:

$$\eta^2 = -\frac{1}{3} II \tag{33}$$

$$\xi^3 = \frac{1}{2}\, III \tag{34}$$

The realizability conditions (Schumann, 1977) are:

- $R_{ij} \geq 0 \;\; (i = j)$ non-negative turbulent energies,
- $R_{ij}^2 \leq R_{ii} R_{jj}$ the cross correlation between velocity fluctuations is bounded by the magnitude of autocorrelations,
- $\det(R_{ij}) \geq 0$ Reynolds stress tensor must be real.

As real and symmetric matrix, the anisotropic stress tensor can be diagonalized, in the frame of its principal axis, by an orthonormal matrix (Simonsen and Krogstad, 2016):

$$B = X\Sigma X^T \tag{35}$$

Where $\Sigma = diag(\sigma_1, \sigma_2, \sigma_3)$ is a diagonal matrix with σ_i the matrix *B* eigenvalues, *X* = <*x'*,*y'*,*z'*> is the orthonormal basis corresponding to the principal axes (eigenvectors).

By changing the old coordinate system (*x*,*y*,*z*) in a new coordinate system (*x'*,*y'*,*z'*), coinciding with the principal axis of the tensor (eigenvectors), the anisotropic tensor became a diagonal tensor with the principal normal stresses on the diagonal (eigenvalues) and the turbulent shear stresses zero. A graphical representation of the tensor state is also possible.

By mapping a unit sphere in the old coordinate system to the eigenvector space, we have (Simonsen and Krogstad, 2016):

$$\left(\frac{x'}{\sigma_1}\right)^2 + \left(\frac{y'}{\sigma_2}\right)^2 + \left(\frac{z'}{\sigma_3}\right)^2 = 1 \tag{36}$$

This describes the shape of the energy sphere in the new system principal axis, where shear stresses are zero.

The shape of the characteristics spheroid is determined by its radii which correspond to the eigenvalues of the matrix and it is rotated with respect to the old coordinate system by the transformation imposed by the rotation matrix *X*.

Table 2 reports the limits of the realizable states for the Reynolds stress tensor in the Lumley triangle map. Figure 6 presents the Lumley triangle with the axisymmetric state region.

State of turbulence	Invariants	Eigenvalues	Shape
Isotropic	$\eta = \xi = 0$	$\sigma_1 = \sigma_2 = \sigma_3 = 0$	Sphere
Two components axisymmetric	$\eta = -1/6, \xi = 1/6$	$\sigma_1 = \sigma_2 = 1/6$	Disk
One component	$\eta = \xi = 1/3$	$\sigma_1 = 2/3, \sigma_2 = \sigma_3 = -1/3$	Line
Axisymmetric (one large eigenvalue)	$\eta = \xi$	$-\frac{1}{3} \leq \sigma_1 = \sigma_2 \leq 0$	Prolate spheroid (Rod-like)
Axisymmetric (one small eigenvalue)	$\eta = -\xi$	$0 \leq \sigma_1 = \sigma_2 \leq 1/6$	Oblate spheroid (Disk-like)
Two components	$\eta = (1/27 + 2\xi^3)^{1/2}$	$\sigma_1 + \sigma_2 = 1/3$	Ellipse

Table 2 Realizability boundaries of the Lumley triangle. (Pope, 2000)

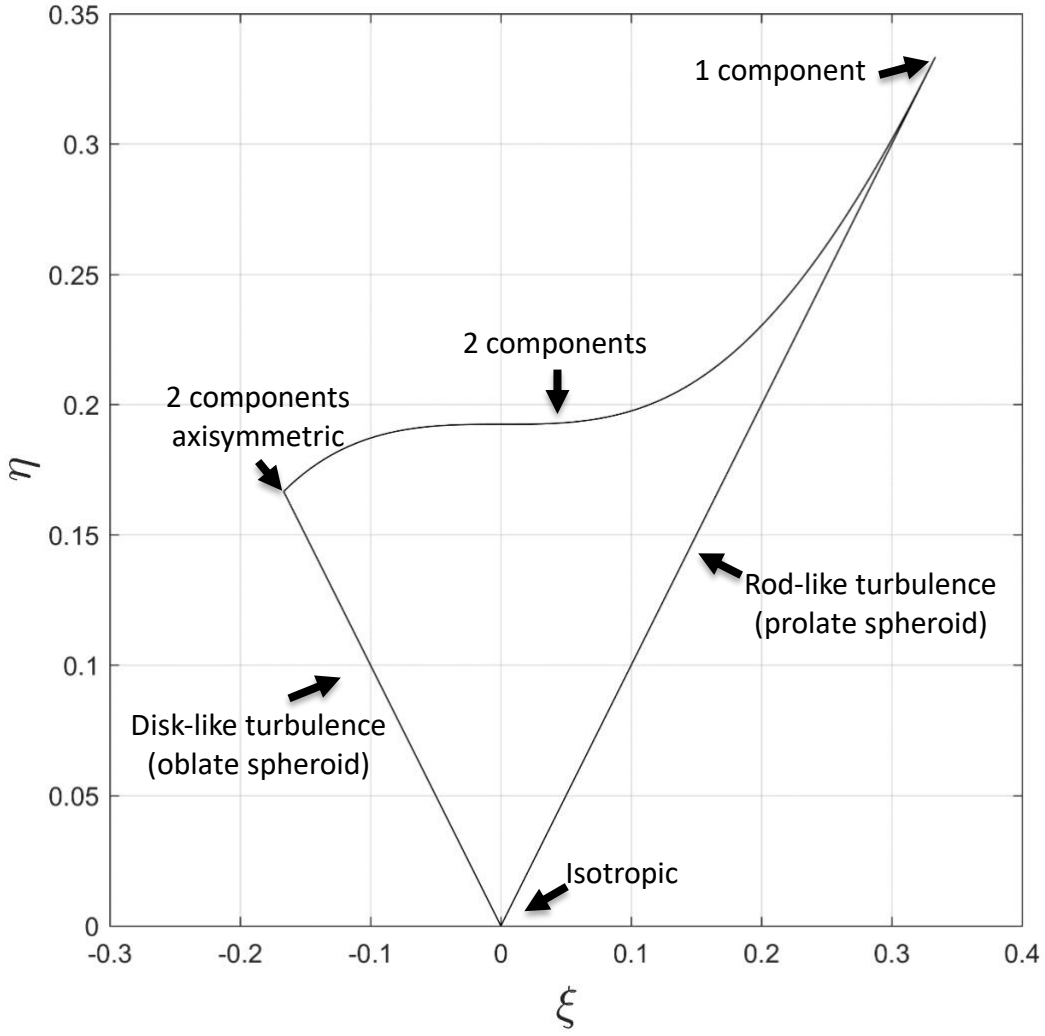

Figure 5 Lumley triangle. States of turbulence.

6. RESULTS AND DISCUSSION

6.1. PANS model verification and validation

The validation and verification will be performed on vertical and horizontal planes of the computational domain. Several quantities of interests will be analyzed.

6.1.1. Vertical Planes

In this section, we present the profiles of the three velocity components (V_x, V_y, V_z) on two vertical planes at different elevations (Figure 1) as well as the variance and covariance of the fluctuating velocity flow fields.

We extracted the data from these locations in order to compare our simulation results with the experimental data. Figure 7 shows the instantaneous scalar velocity magnitude on Plane 1. It can be observed that as the PANS filter becomes smaller, the flow field structure tends to approach the same degree of resolution as that of the LES model. The URANS model is incapable of reducing the eddy viscosity during the course of the simulations. The unresolved scales of motion create excessively large values of turbulent viscosity, which will damp all types of flow instabilities, producing a quasi-steady RANS solution. The subsequent decrease in the PANS filter ($f_k = 0.8$ and $f_k = 0.6$) results in liberation of the largest scales of motion in the region downstream of the spacer grid while keeping the region within proximity of the mixing vanes frozen to the

quasi-steady RANS solution. As the PANS filter becomes smaller, it can be observed that the spectrum of the resolved scales increases even in regions close to the spacer grid and tips of the mixing vanes. Indeed, this observation is characteristic of a bridging model, where it is possible to continuously span all scales in the turbulent kinetic energy spectrum.

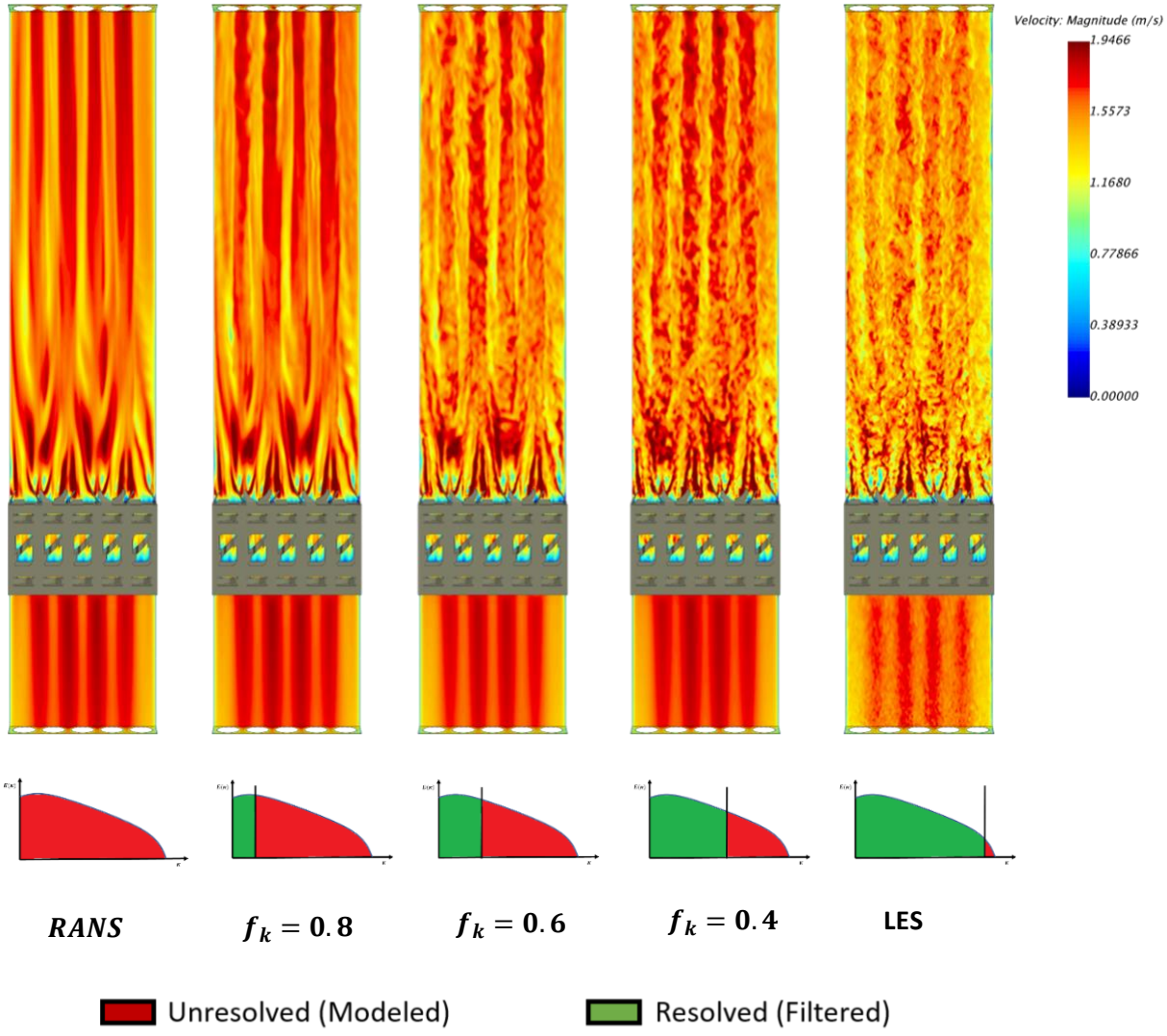

Figure 6 Instantaneous scalar velocity magnitude representation on Plane 1.

6.1.1.1. First and Second-Order Turbulence Statistics

Figure 8 and Figure 9 show the time-averaged velocity component profiles on Plane 1 and Plane 2, respectively, taken from selected elevations. The time-averaged velocity component profiles are expressed in terms of hydraulic diameter D_h with respect to the mixing vane tip. It can be observed that the velocity component profiles tend to approach the resolution of the LES model as the PANS filter becomes smaller. The differences between the PANS and LES model results are not as marked, except for some local regions, which can be attributed to the flow physics at low Reynolds number, where the turbulence statistics only have a marginal effect on the mean of the velocity (first-order statistics) flow field.

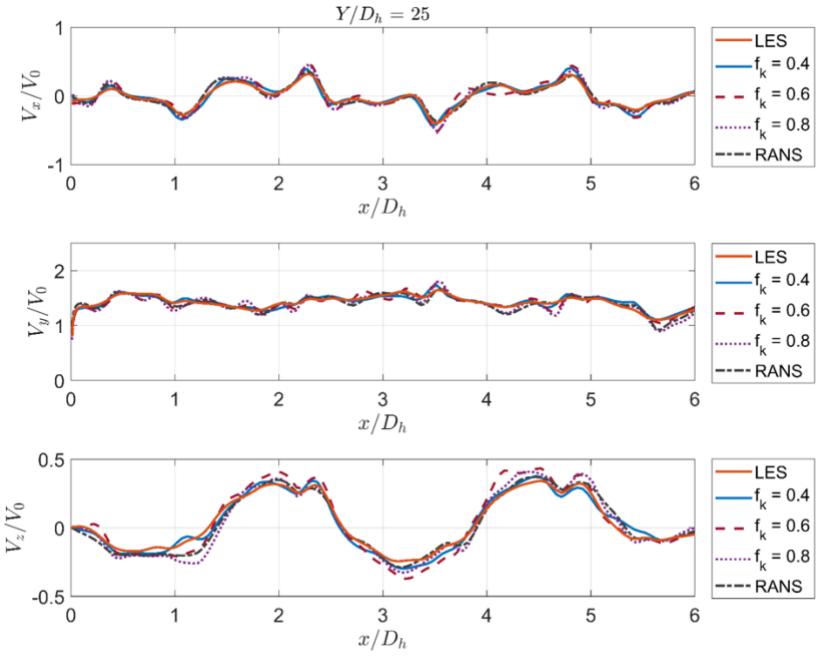

Figure 7 Time-averaged velocity component profiles on Plane 1.

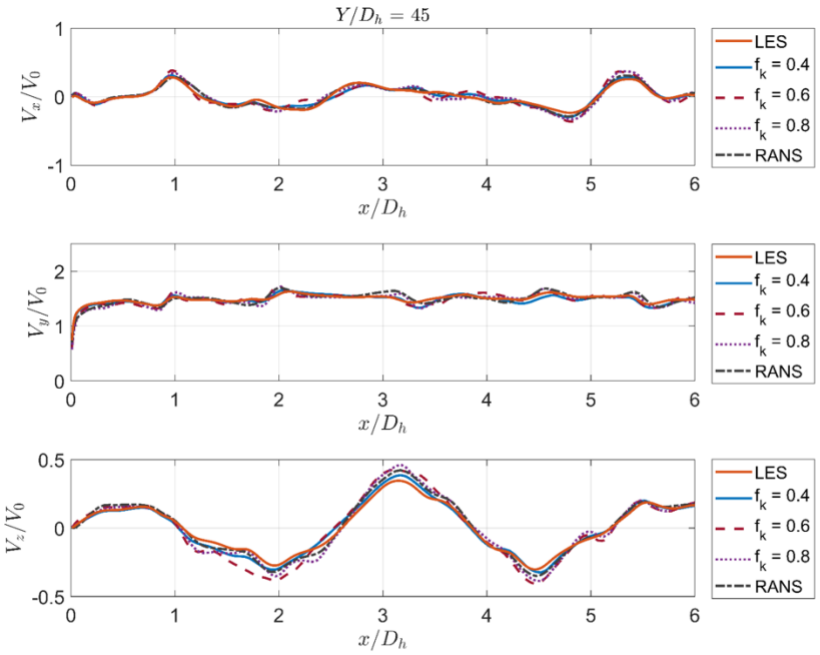

Figure 8 Time-averaged velocity component profiles on Plane 2.

The differences are more pronounced for the second-order statistics of the resolved flow field, as expected. Figure 10 and Figure 11 show the variance and covariance of the resolved fluctuating velocity field and the sum of the resolved and modeled components:

$$\langle V_i' V_j' \rangle^{Tot} = \langle V_i' V_j' \rangle^{Res} + \langle V_i' V_j' \rangle^{Mod} \tag{37}$$

where the modeled component of the second-order statistics of the flow field is based on the Boussinesq approximation.

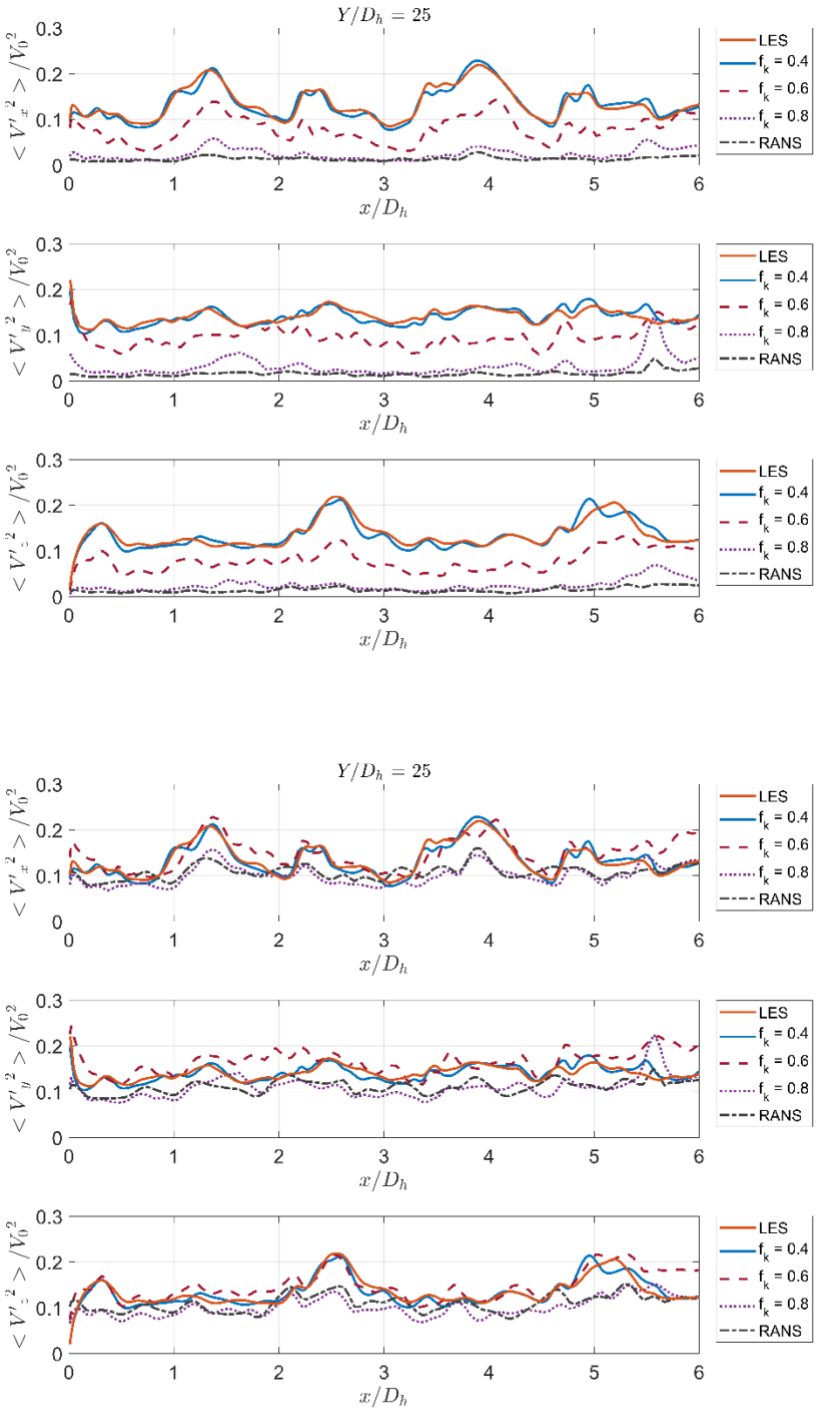

Figure 9 Variance of the velocity component profiles on Plane 1. Resolved components (top). Sum of the modeled and resolved components (bottom).

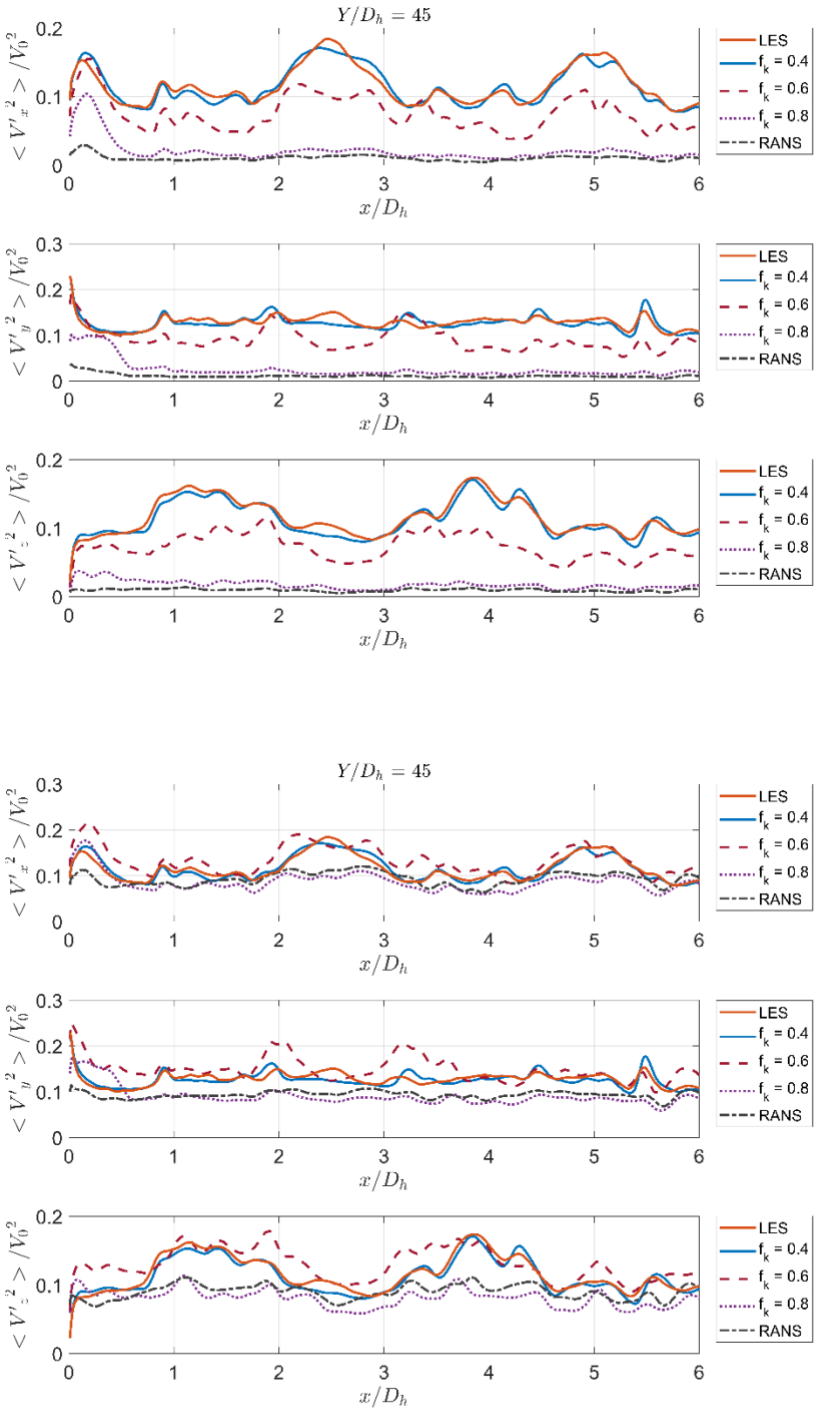

Figure 10 Variance of the velocity component profiles on Plane 2. Resolved components (top). Sum of the modeled and resolved components (bottom).

It can be seen that the second-order statistics of the resolved velocity field (top of Figures 10-11) tends to be almost zero for the URANS model because all of the turbulence spectrum is modeled. In addition, the resolved second-order statistics tend to approach those for the LES model as the PANS filter becomes smaller. This is in complete agreement with the PANS model paradigm.

The overall turbulence statistics (bottom of Figures 10-11), i.e., sum of the resolved and modeled flow fields, tends to be underpredicted for the PANS model with the largest filters, compared with those for the LES model. This is mainly due to the linear constitutive relationship (μ_t isotropy) between the Reynolds stresses and strain rates (Boussinesq approximation), which has a significant impact on the results for such filters, especially in regions with strong secondary flow structures.

A similar behavior can be observed for the covariance of the fluctuating velocity flow field, as shown in Figure 12.

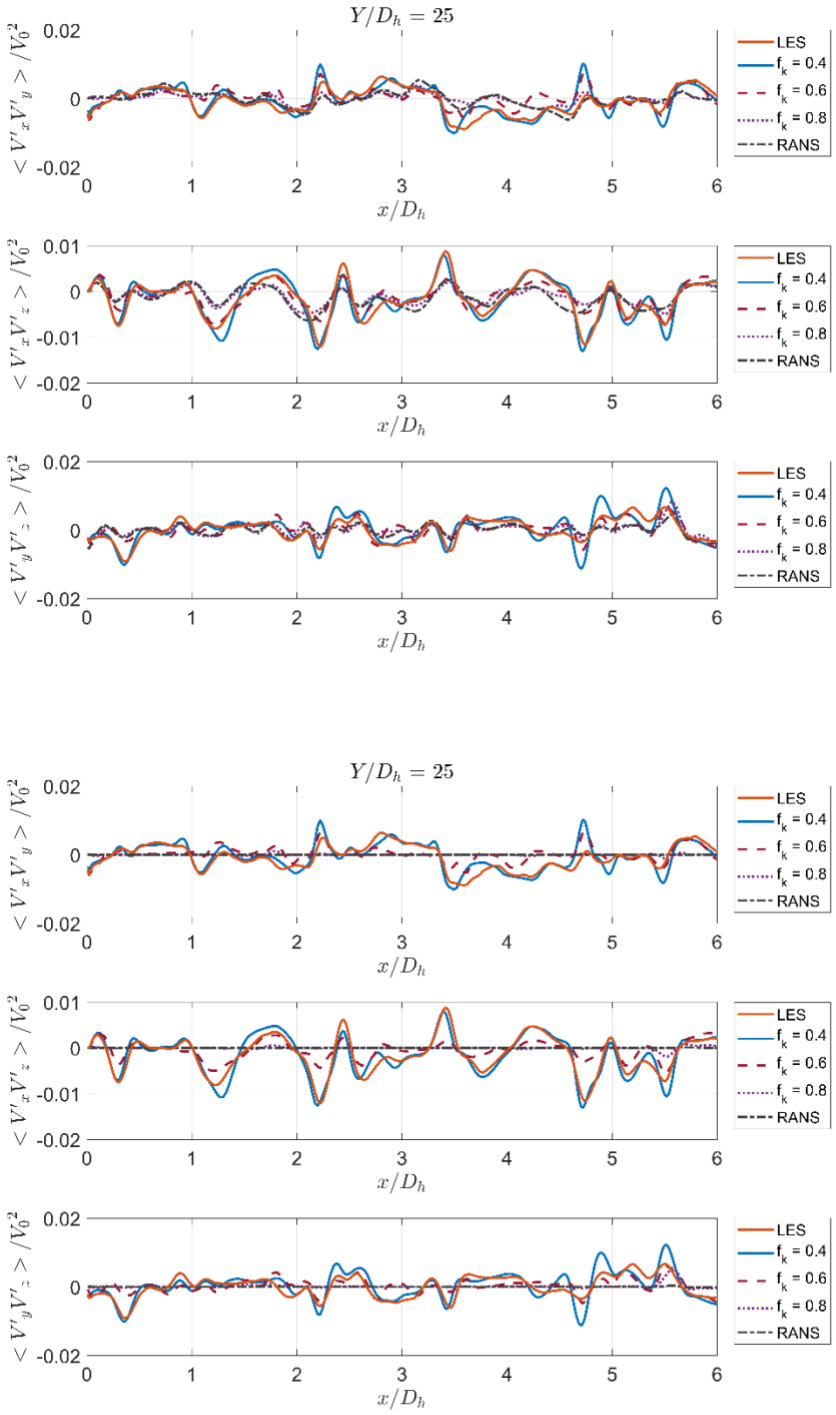

Figure 11 Covariance of the velocity component profiles on Plane 1. Resolved components (top). Sum of the modeled and resolved components (bottom).

6.1.1.2. A posteriori PANS consistency criterion

We imposed the dissipation filter to be $f_\epsilon = 1$ and thus, the recovery ratio becomes $f_\nu = f_k^2$. The three PANS filters ($f_k = 0.8$, $f_k = 0.6$, and $f_k = 0.4$) result in a recovery ratio of $f_\nu = 0.64$, $f_\nu = 0.36$, and $f_\nu = 0.16$, respectively, which will be used for the internal consistency test.

We evaluated the distribution of the recovery ratios for our simulations on Plane 1 and Plane 2 in the region downstream of the spacer grid, regions selected because of interest for validation with experiments purposes. Figure 13 shows the results on Plane 1.

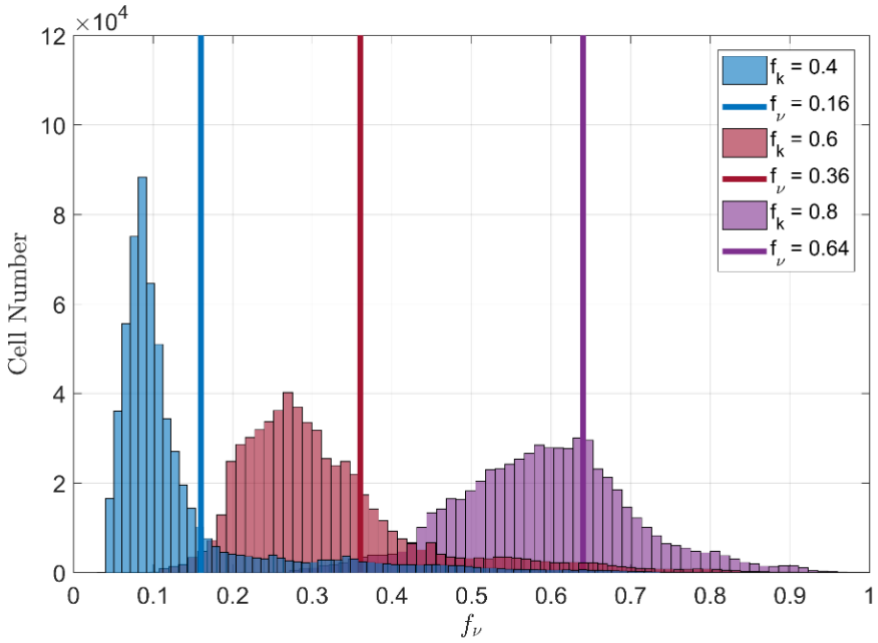

Figure 12 Distribution of the recovery ratios on Plane 1 for different PANS filters.

The vertical lines represent the externally imposed recovery ratios f_ν whereas the histograms represent the distribution of the recovery ratios on each plane cell. It should be noted that these results are obtained from the coarse mesh simulations. It can be observed that the simulations tend to underpredict the recovery ratios (or in other words, the recovery ratios on each plane cell are less than the externally imposed ones), which indicates that the spatial discretization is inadequate, especially for the smallest PANS filter. Due to the inadequate spatial discretization, we performed mesh refinement for the smallest PANS filter ($f_k = 0.4$) in order to evaluate the effects of such refinement on the internal consistency of the closure model.

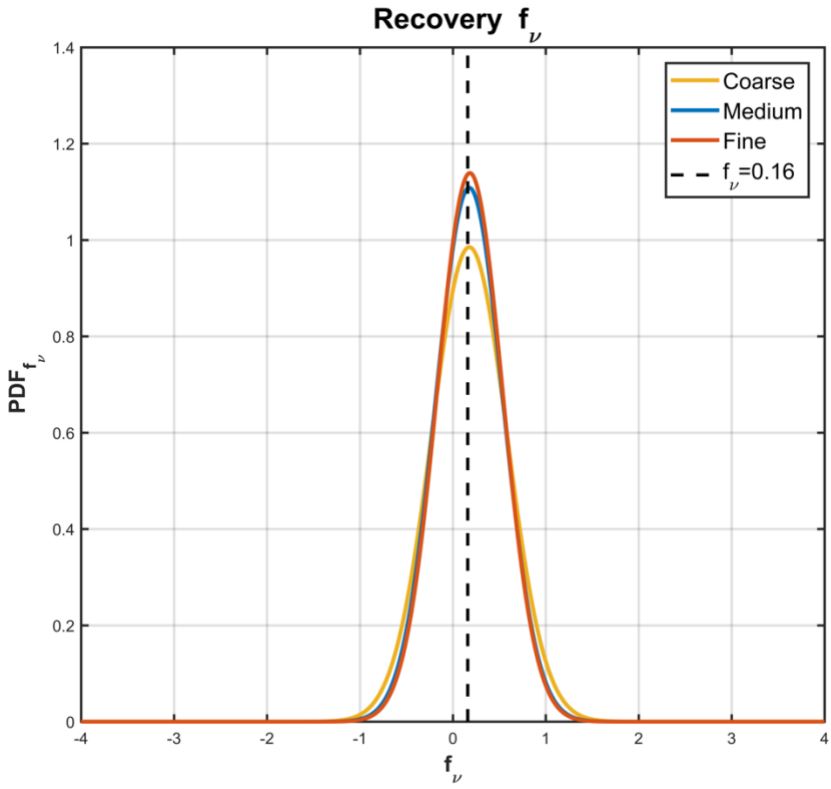

Figure 13 Distribution of the recovery ratio distribution on Plane 1 after mesh refinement for fk = 0.4.

It can be observed from Figure 14 that there is a reasonable shift in the recovery ratio f_ν distribution toward the externally imposed recovery ratio ($f_\nu = 0.16$), indicating that the previous spatial discretization (coarse mesh) is indeed inadequate for the smallest PANS filter.

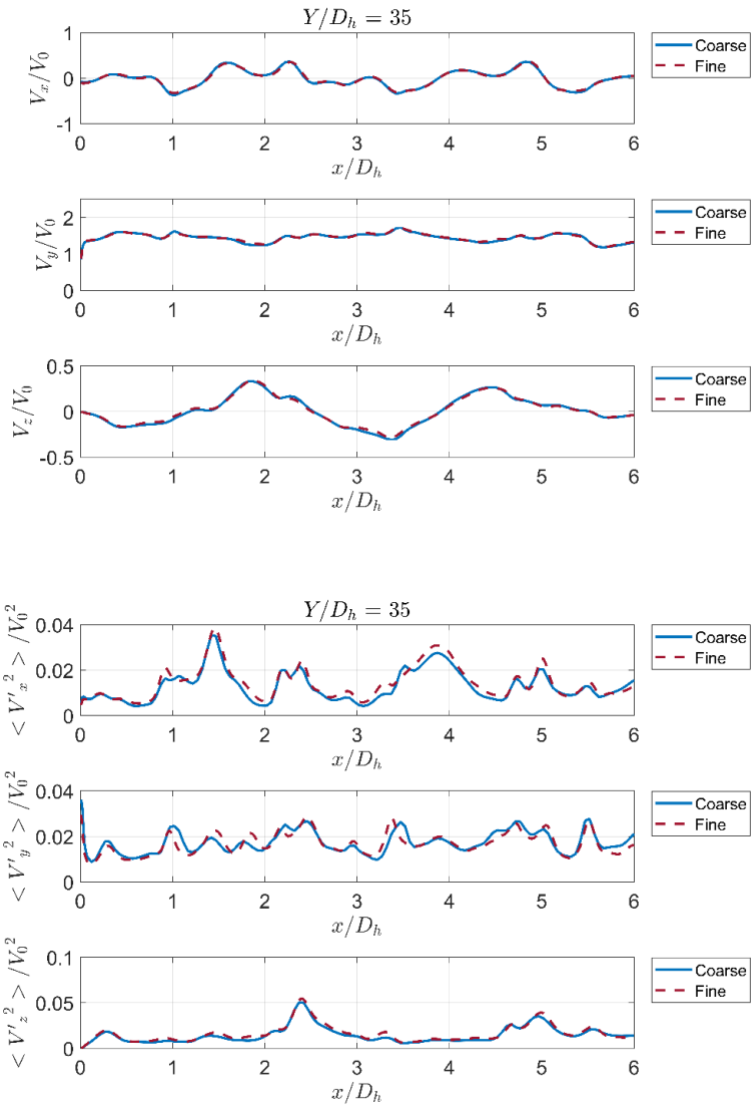

Figure 14 Mesh refinement on plane 1. Velocity (TOP) RMS (BOTTOM).

In addition, it is found that the mesh refinement does not affect the mean velocity field, but slightly increases the local resolution of the second-order statistics of the flow. Figure 15 shows the time-averaged velocity component profiles and variance of the velocity component profiles on Plane 1 for the coarse and fine mesh cases.

6.1.1.3. Numerical solution verification

The numerical discretization error has been estimated for both local and global quantities. Time average velocity and variance profiles, for the three components of the velocity have been evaluated and compared with PIV experimental results.

The profiles have been taken on one of the vertical planes in the downstream region of the spacer grid. The experimental uncertainty has been also highlighted. Figure 16 and Figure 17, presents some of the line profiles at two different elevations. Comparison with LES model is present within the same plots. Each line profile comes together with the PDF distribution of the observed order of accuracy. In all the cases the PDF peak was lying around the imposed numerical order $p = 2$ of the discretization scheme.

Comments about the numerical model validation will be presented in the next section.

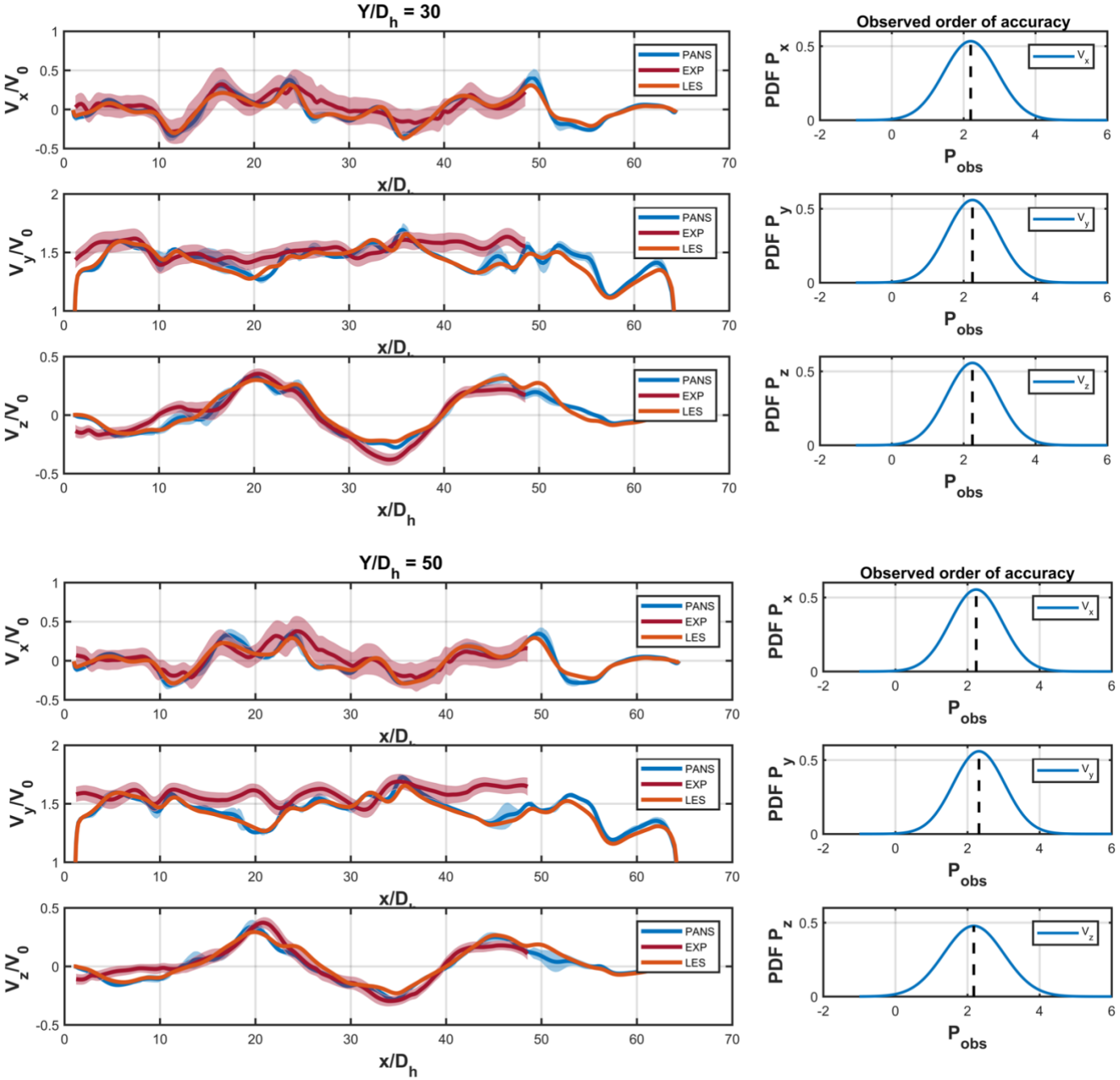

Figure 15 Velocity profiles at two elevations (y/Dh =3 top, y/Dh =5 bottom). Shaded area GCI (blue), experimental uncertainty (red). (PANS filter fk=0.4).

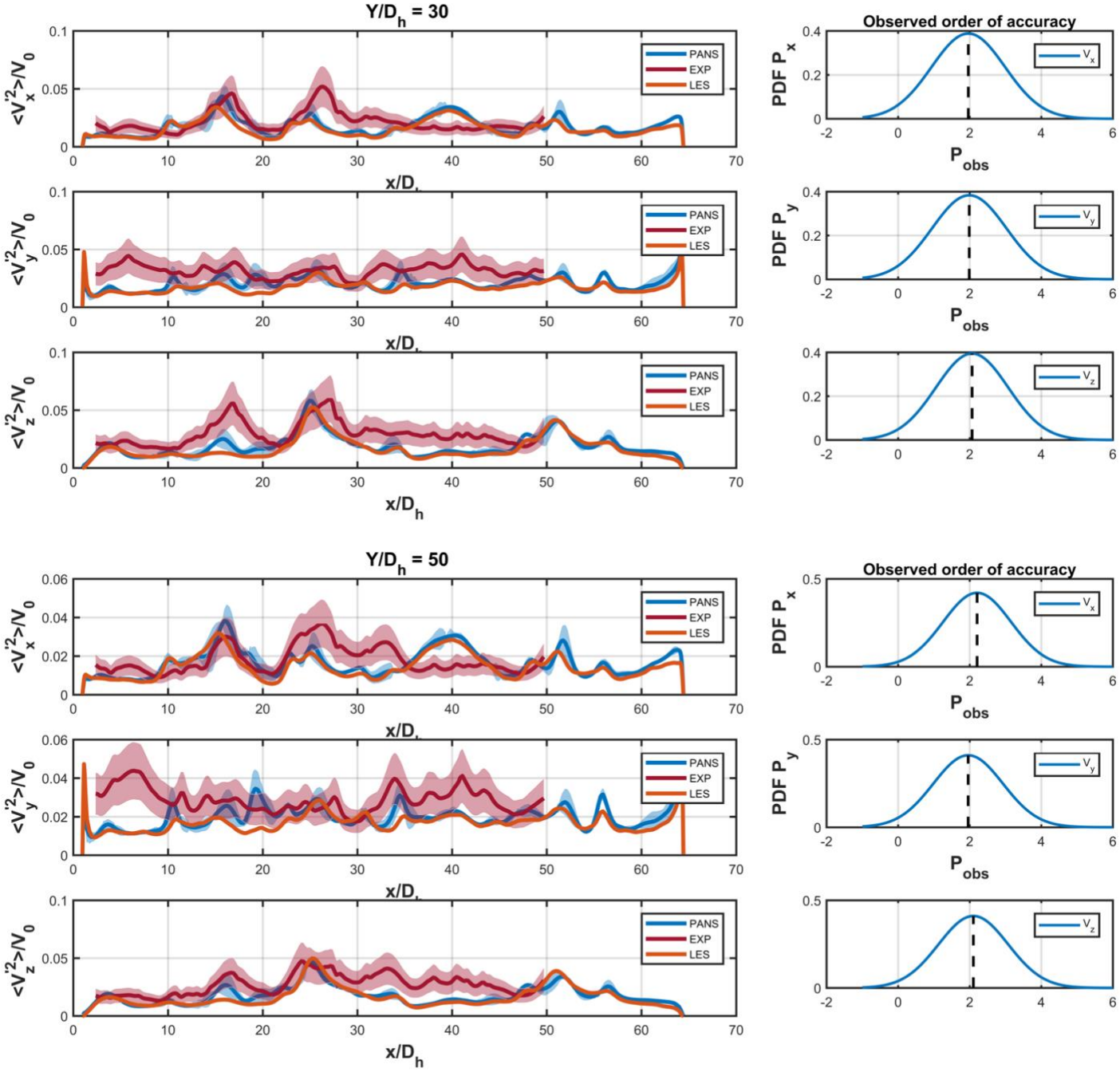

Figure 16 Velocity variance profiles at two elevations (y/Dh =30 top, y/Dh =50 bottom). Shaded area GCI (blue), experimental uncertainty (red). (PANS filter fk=0.4).

6.1.1.4. Validation with experimental data

Figure 18 and Figure 19 show the comparison of the time-averaged velocity component profiles and root-mean-square velocity components profiles, between the numerical models and PIV results of (Nguyen and Hassan, 2017) on Plane 1. According to them, the overall estimated uncertainty of PIV measurements was less than 5% of the mean axial velocity in the fuel bundle flow. Further details of the PIV measurements can be reviewed in (Nguyen and Hassan, 2017). It can be seen that there is good agreement in the time-averaged velocity component profiles between the numerical models (LES and PANS models) and PIV data. In general, the trends of the time-averaged velocity component profiles are similar; however, there is a slight difference in the trend for the vertical component V_y. The first-order turbulence statistics are not significantly influenced by the turbulent flow structure due to the flow physics at low Reynolds number. Indeed, we have observed this behavior when we compared the first-order turbulence statistics between the PANS and LES models. In contrast, there is a larger difference in the second-order turbulence statistics between the numerical models and PIV data. It can be observed that spurious peaks are present in the PIV data while in other cases, there are no peaks present in the PIV data compared to the numerical results.

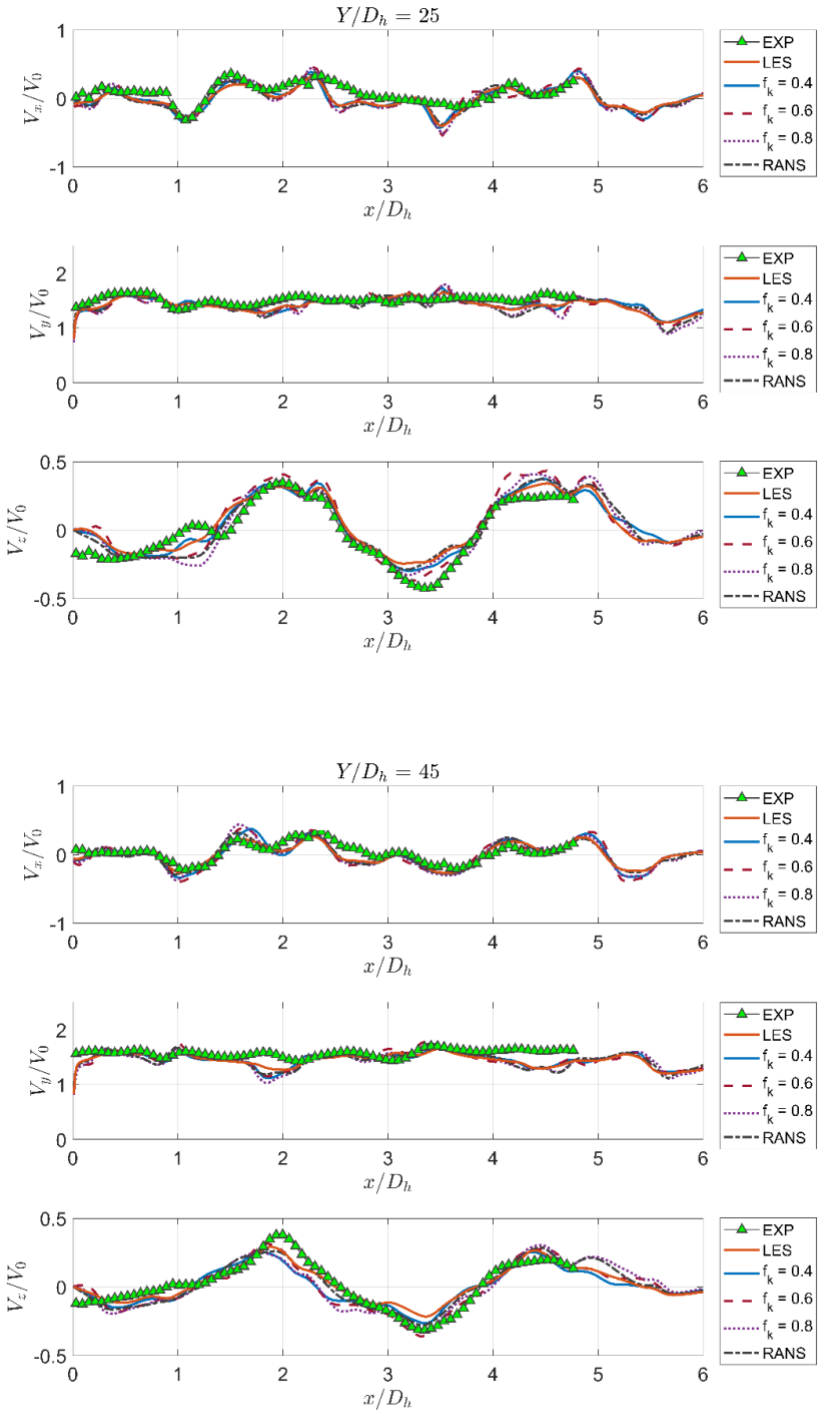

Figure 17 Time-averaged velocity component profiles on Plane 1.

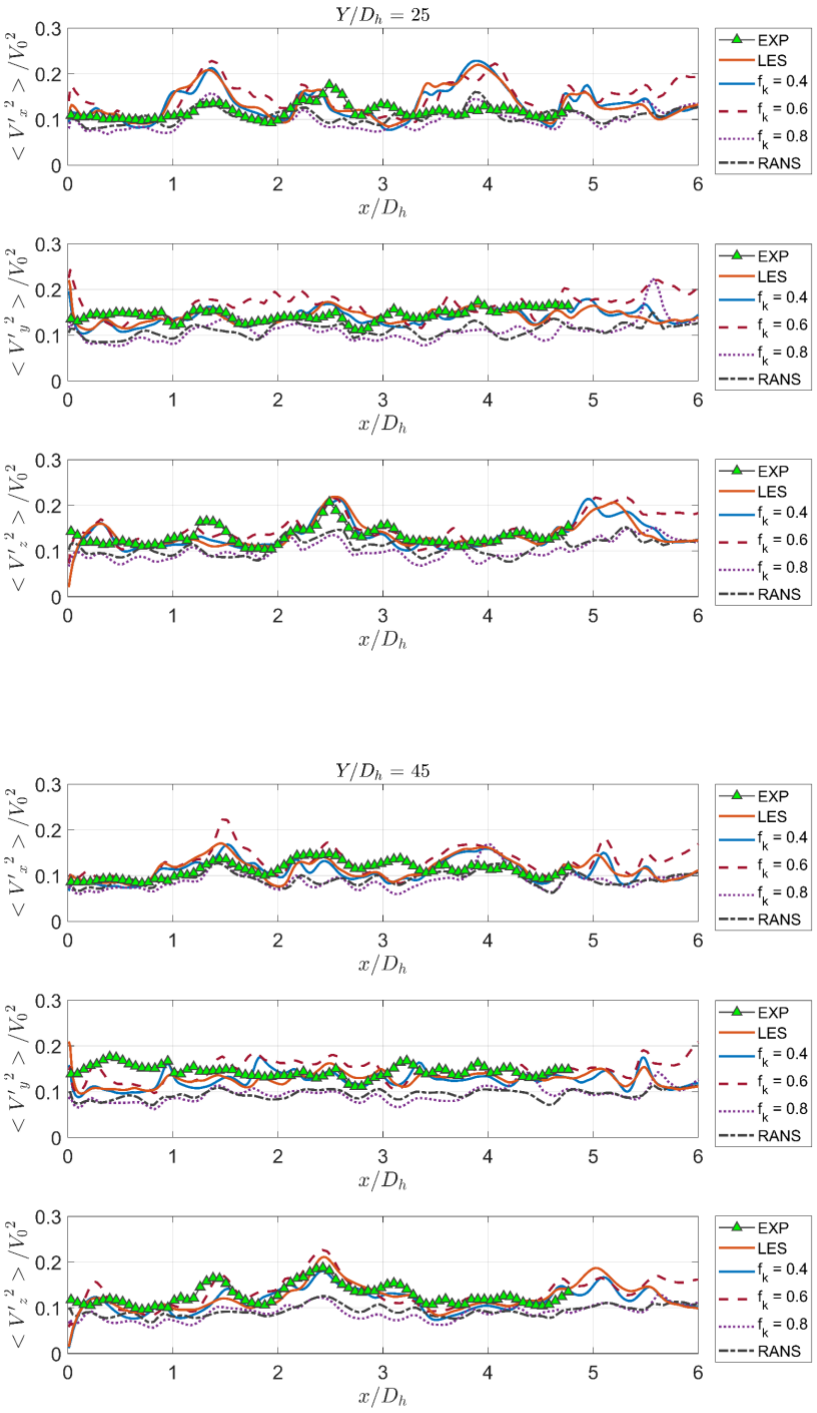

Figure 18 RMS of the velocity component profiles on Plane 1.

In general, the LES model and PANS model with the smallest filter ($f_k = 0.4$) have a higher degree of resolution compared to the other models, where the time-averaged velocity component profiles and RMS magnitudes are comparable to those from the PIV experiments. In contrast, the URANS model and PANS model with larger filters ($f_k = 0.6, f_k = 0.8$) tend to underestimate the time-averaged velocity components and RMS of the velocity components.

As introduced in the previous section, a model validation metrics has been introduced to quantify and monitor the performance of the LES and PANS models.

Figure 20 presents the results on Plane1, the same trend was observed on Plane2. Here we have addressed RANS simulation with $f_k = 1$ and LES as $f_k = 0.1$. As can be observed for both cases, the relative validation error tends to decrease as the resolution of the turbulent flow field increases for both MKE and TKE.

The metrics also shows that in the region close to the spacer grid the MKE tends to have the smallest relative error (e.g. $y/D_h = 25$) and TKE tends to have the largest error, especially for smallest filters f_k.

The differences in the first-order and second-order turbulence statistics between the numerical models and PIV experiments may be attributed to the following reasons.

The first one is uncertainties in the geometrical representation. Since the mixing vanes of the spacer grid are subjected to deformations (which can occur during assembly of the test section or continuous testing of the facility at different Reynolds numbers) and since the vane orientation plays a crucial role in the development of secondary flows as

well as the turbulent flow structure itself, it is very likely that the computer aided design model of the fuel rod bundle configuration is not a perfect representation of the real one.

The second reason that will lead to discrepancies between the numerical and experimental results is the boundary conditions. In the actual facility, three support grids are present prior to the spacer grid under investigation, which will influence the flow characteristics upstream of the spacer grid. It shall be noted that in all of the simulations in this study, we imposed a fully developed flow velocity profile obtained from precursor runs of the bare rod bundle using LES.

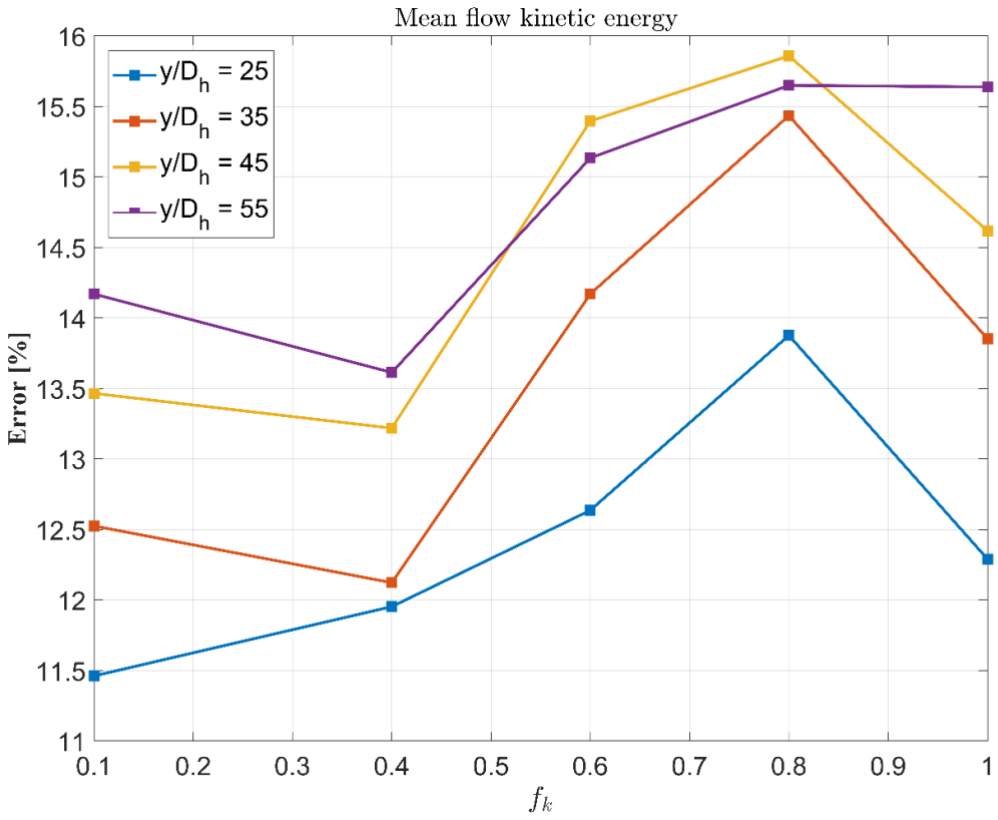

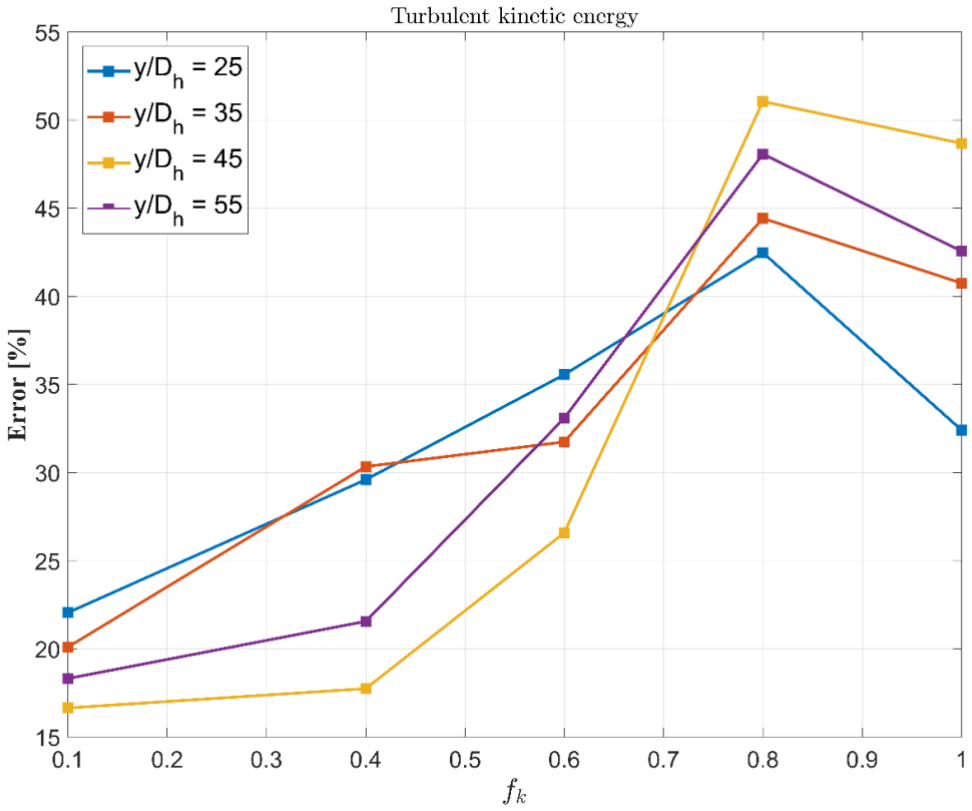

Figure 19 Validation metrics results on Plane 1 at different downstream locations. Mean flow kinetic energy (top). Turbulent kinetic energy (bottom).

In Table 3 we have reported the overall computational time, in terms of CPU/hours spent for each case corresponding to a different filter f_k.

CASE	CPU/hours
$f_k = 1.0$	5,000
$f_k = 0.8$	23,000
$f_k = 0.6$	174,000

$f_k = 0.4$	490,000
LES ($f_k = 0.1$)	730,000

Table 3 Computational time for each case

6.1.2. Horizontal Planes

Figure 21 shows the locations of the horizontal planes in the upstream and downstream regions of the spacer grid from which the numerical results are derived.

The results obtained from these sections give important information regarding the turbulent flow structure (particularly, the structure of secondary flows) induced by the presence of the spacer grid.

Based on the results, we will draw some conclusions about the origins of the cross flow and we will compare the results obtained from the PANS and LES models.

Most of the results are presented in terms of area-averaged quantities, where we applied the area-average operator on a series of horizontal planes displaced in the downstream region:

$$A_{avg}\langle\cdot\rangle = \frac{1}{A}\sum_i A_i \langle\cdot\rangle \tag{38}$$

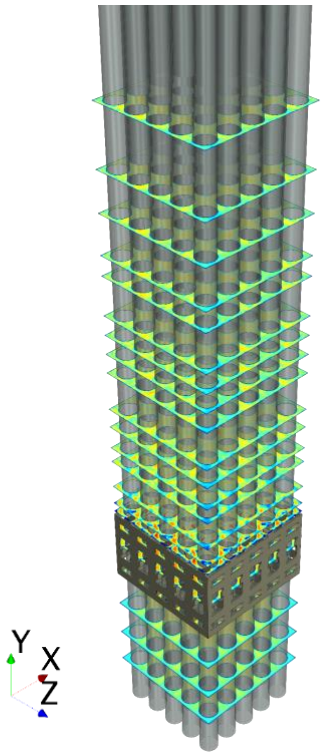

Figure 20 Locations of the horizontal planes in the upstream and downstream regions of the spacer grid

6.1.2.1. Secondary flow intensities

The first quantity of interest is the area-averaged secondary flow intensity (*SFI*) which is defined as:

$$SFI = \frac{1}{A}\sum_i \frac{A_i\sqrt{{V_x}^2+{V_z}^2}}{\overline{V_y}} \tag{39}$$

This quantity is one of the key parameters that can be used to evaluate the effect of the spacer grid on the fluid flow patterns.

The grid itself and the structure of the mixing vane tips will generate strong secondary flow intensities downstream of the vanes. As discussed previously, the presence of the spacer grid disrupts the symmetry of the fully developed flow, which enhances inter-channel flow mixing.

In essence, the secondary flow intensity gives the area-averaged ratio between the in-plane magnitude of the two spanwise velocity components $\bar{V}_{hor} = \sqrt{V_x{}^2 + V_z{}^2}$ and the mean streamwise velocity component $\overline{V_y}$.

High secondary flow intensities promote inter-channel mixing of the coolant inside the fuel rod bundle, which boosts the heat transfer efficiency.

The larger the secondary flow intensity peak, the slower its streamwise decay, which increases the heat transfer efficiency due to the presence of the spacer grid.

Figure 22 shows the comparison between the area-averaged secondary flow intensities on 30 horizontal planes obtained from the PANS and LES models.

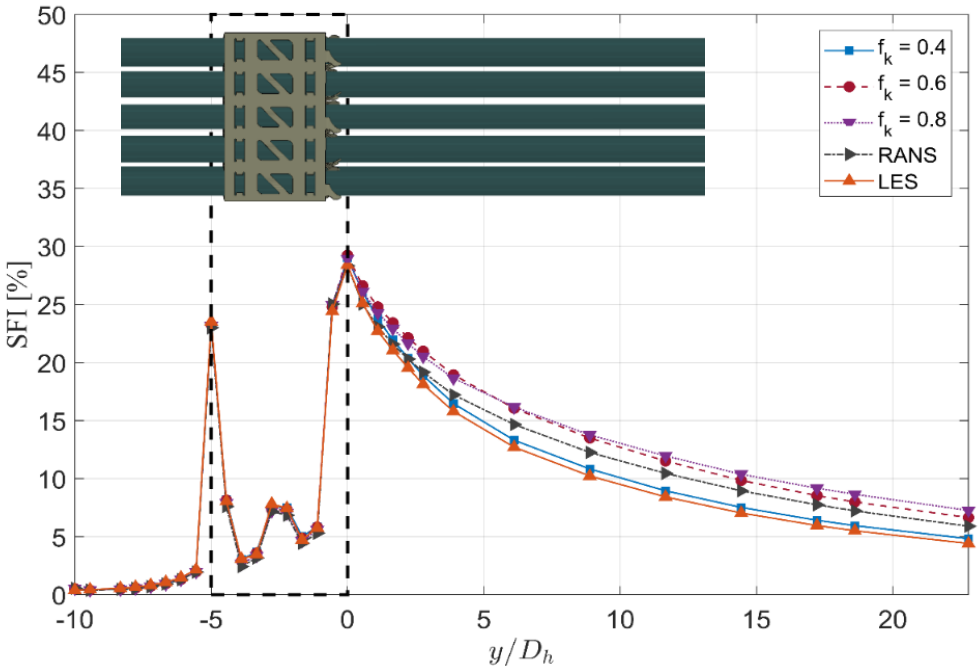

Figure 21 : Secondary flow intensity profiles across the spacer grid

It can be observed from Figure 22 that there are three distinctive peaks. The first peak is due to the bottom of the spacer grid whereas the second peak is due to the presence of the springs and dimples at the spacer grid/bundle interface.

The third peak (which also has the highest magnitude) is due to the presence of the split-type mixing vanes at the top of the spacer grid. It can be seen that the PANS model with the smallest filter ($f_k = 0.4$) gives the same peak magnitude and decay rate as those for the LES model.

The other PANS filters ($f_k = 0.6, f_k = 0.8$) tend to overestimate the secondary flow intensities, resulting in a slower decay rate.

Figure 23 shows the structure of the secondary flow at different elevations obtained from the LES model. It is evident from analysis of the secondary flow downstream of the spacer grid that there are three types of flow behavior. In the region immediately after the mixing vanes, two energetic small vortex structures, rotating in opposite direction, are generated in the middle of each subchannel by two adjacent vanes, as shown in Figure 23a.

These rotating vortex structures induce shear forces (as indicated by the red arrows in Figure 23c) at the vortex/flow interface, which accelerates the surrounding fluid and promotes cross flow in the fuel rod bundle.

The rotating vortex structures become larger and less energetic as they transfer their momentum to the surrounding flow (Figure 23e) and these vortex structures eventually merge to form a single vortex, which decreases the secondary flow intensity.

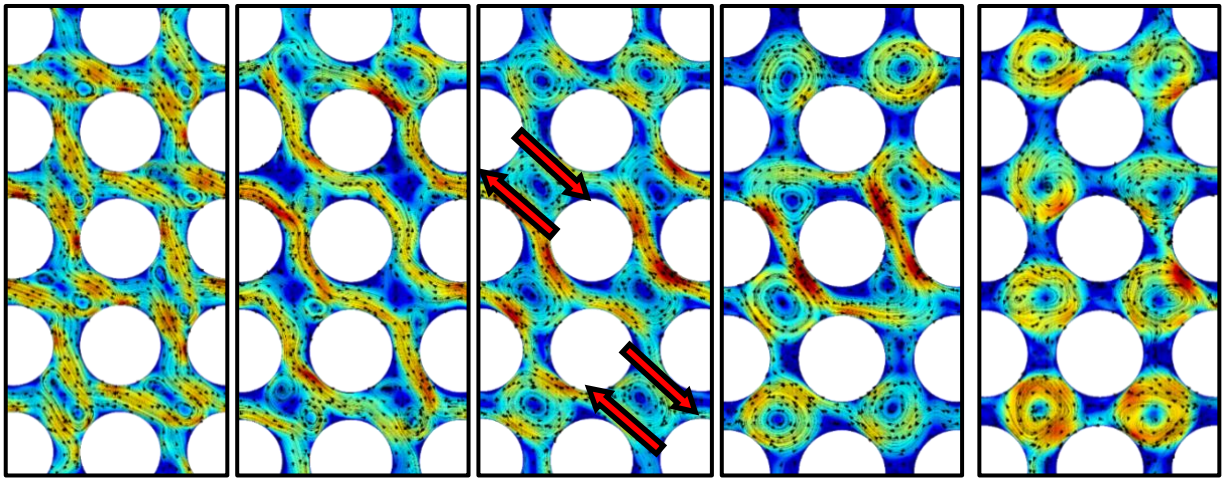

Figure 22 Structure of the secondary flow at different elevations obtained from the LES model. y/Dh = 1 (a). y/Dh = 3 (b). y/Dh = 5 (c). y/Dh = 7 (d). y/Dh = 10 (e).

The flow physics, characterized by vortex stretching and continuous remodeling, can be the cause of failure of the standard two-equation RANS model, where the closure model is based on the linear relationship between the Reynolds stress and strain rate tensors.

The reduction of the PANS energy-based filter f_k, confines the influence of the Boussinesq closure relation to the smaller scales of motion.

In this manner, the larger turbulent scales, which are strongly influenced by the system geometry and boundary conditions (and therefore, difficult to model) will be directly resolved. At the same time, the smaller turbulent scales at the end of the inertial subrange tend to be closer to the region where the so-called "universal equilibrium" (Kolmogorov's theory) can be easily represented by the Boussinesq approximation.

This region is the range of turbulent scales where the turbulent flow structure is independent of the flow geometry. This is the same approach used in LES; however, the continuous filtering option provided by PANS modeling gives a more flexible, grid-independent choice of resolution.

6.1.2.2. Turbulent Kinetic Energy

For scale-resolving simulations using PANS or LES model, the filtering action of the turbulence model generates an unfiltered set of turbulent scales (in case of PANS) or subgrid scales (in case of LES), which needs to be modeled. In LES modeling, the subgrid

scales correspond to all of the unresolved turbulent scales that belong to a non-resolved space due to the discretized domain size $\Delta_{cut-off}$.

In PANS modeling, these non-resolved scales belong to the non-resolved energy space (i.e., turbulent kinetic energy space) imposed by the unresolved-to-total kinetic energy filter f_k.

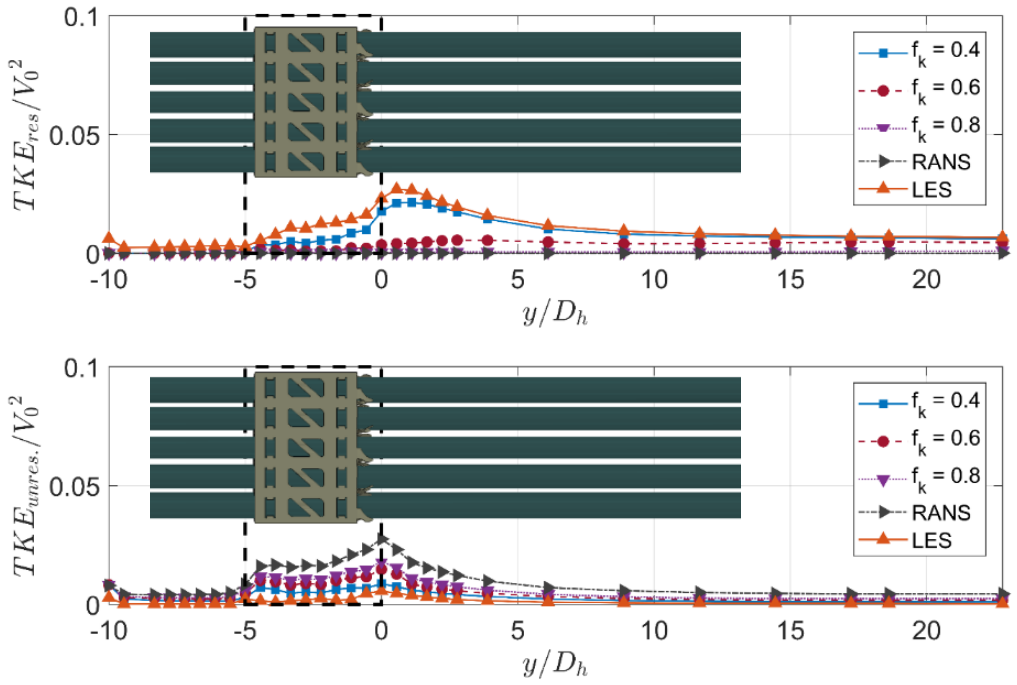

Figure 23 Turbulent kinetic energy profiles across the spacer grid. Resolved (top). Modeled (bottom).

Figure 24 shows the area-averaged resolved and unresolved turbulent kinetic energy profiles. It is apparent that the PANS models obey the bridging computational paradigm, where the unresolved-to-total turbulent kinetic energy filter dictates the continuous shift of the energy based on the cut-off filter within the inertial turbulent scale

range. The resolved turbulent kinetic energy TKE_{res} decreases starting from the $f_k = 0.4$ case down to zero for the $f_k = 1$ case, equivalent to the results of the URANS model. The unresolved turbulent kinetic energy TKE_{unres} (i.e., the modeled component) tends to decrease from the URANS model to the LES model. The TKE_{res} and TKE_{unres} profiles of the LES model are very similar to those for the PANS model with the smallest filter ($f_k = 0.4$).

The total turbulent kinetic energy, sum of the resolved and unresolved component, showed a general underestimation for the largest PANS filters ($f_k = 1, f_k = 0.8, f_k = 0.6$), compared to the LES and $f_k = 0.4$ cases. The results provide physical insight on the flow where the presence of mixing vanes at the top of the spacer grid increases the energy of the turbulent flow structure downstream of the vanes, which decays in the same trend as that for the secondary flow intensity.

6.1.2.3. Horizontal planes Solution Verification

The numerical solution verification has been applied also to integral quantities.

Pressure profiles and secondary flows intensity (SFI) have been evaluated across the spacer grid.

In Figure 25, it can be also observed the difference between the different PANS filters, and their comparison with LES. As it is clear, the PANS model results will tend to the LES resolution as the filter is moved inside the turbulent energy spectrum at larger wavelengths. I

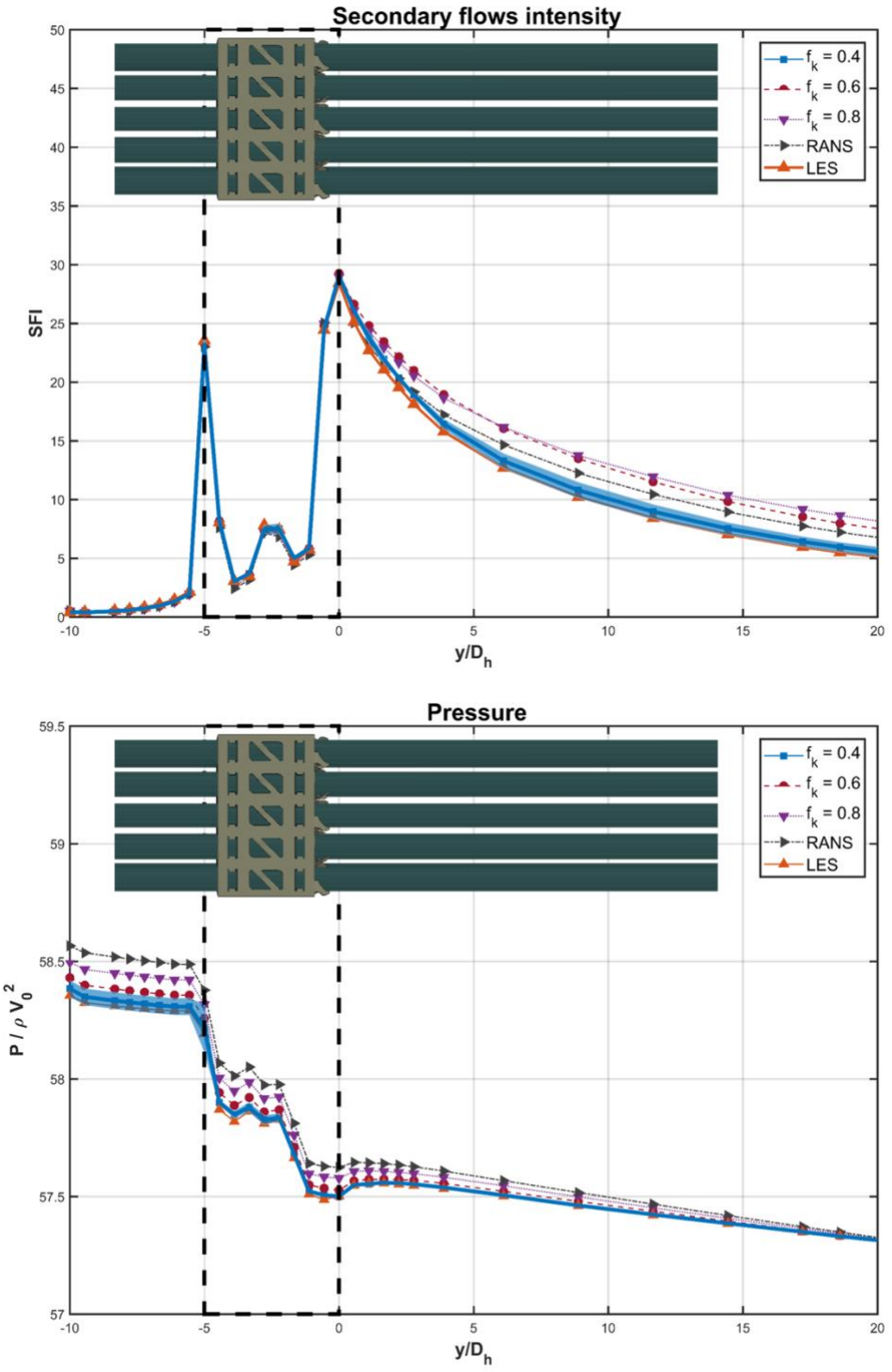

Figure 24 Secondary flow intensity (top). Pressure profiles (bottom). Comparison of different PANS filters with LES. Shaded area GCI for PANS filter fk=0.4.

6.1.2.4. Horizontal planes qualitative comparison with experiments

The background color of the velocity vector fields (Figure 26) for the numerical models (LES model and PANS model with $f_k = 0.4$) and PIV data of (Estrada-Perez et al. 2016) refers to the normalized magnitude of the secondary flow, which is defined by $\sqrt{V_x{}^2 + V_z{}^2}/V_0$. This will give a deeper understanding on the secondary flow patterns. The mean velocity obtained from the PIV experiments is V_0 = 2.66 m/s.

The results are presented for the horizontal planes located at $y = 5D_h$, $y = 10D_h$, and $y = 25D_h$, respectively, from the mixing vane tips. Even though the Reynolds number for the PIV experiments ($\mathrm{Re} = 28{,}000$) is twice the value ($\mathrm{Re} = 14{,}000$) used in the simulations, the secondary flow structure is essentially the same. In the region immediately after the mixing vanes ($y = 5D_h$), two small energetic vortex structures, rotating in the opposite direction, are generated in the middle of each subchannel by the two adjacent vanes. These rotating vortex structures induce shear forces at the vortex/flow interface, which accelerates the surrounding fluid and promotes cross flow in the fuel rod bundle. The rotating vortex structures become larger and less energetic as they transfer their momentum to the surrounding flow. These vortices eventually merge together to form a single vortex with a decrease in the rotating speed, which in turn, decreases the induced secondary cross flow.

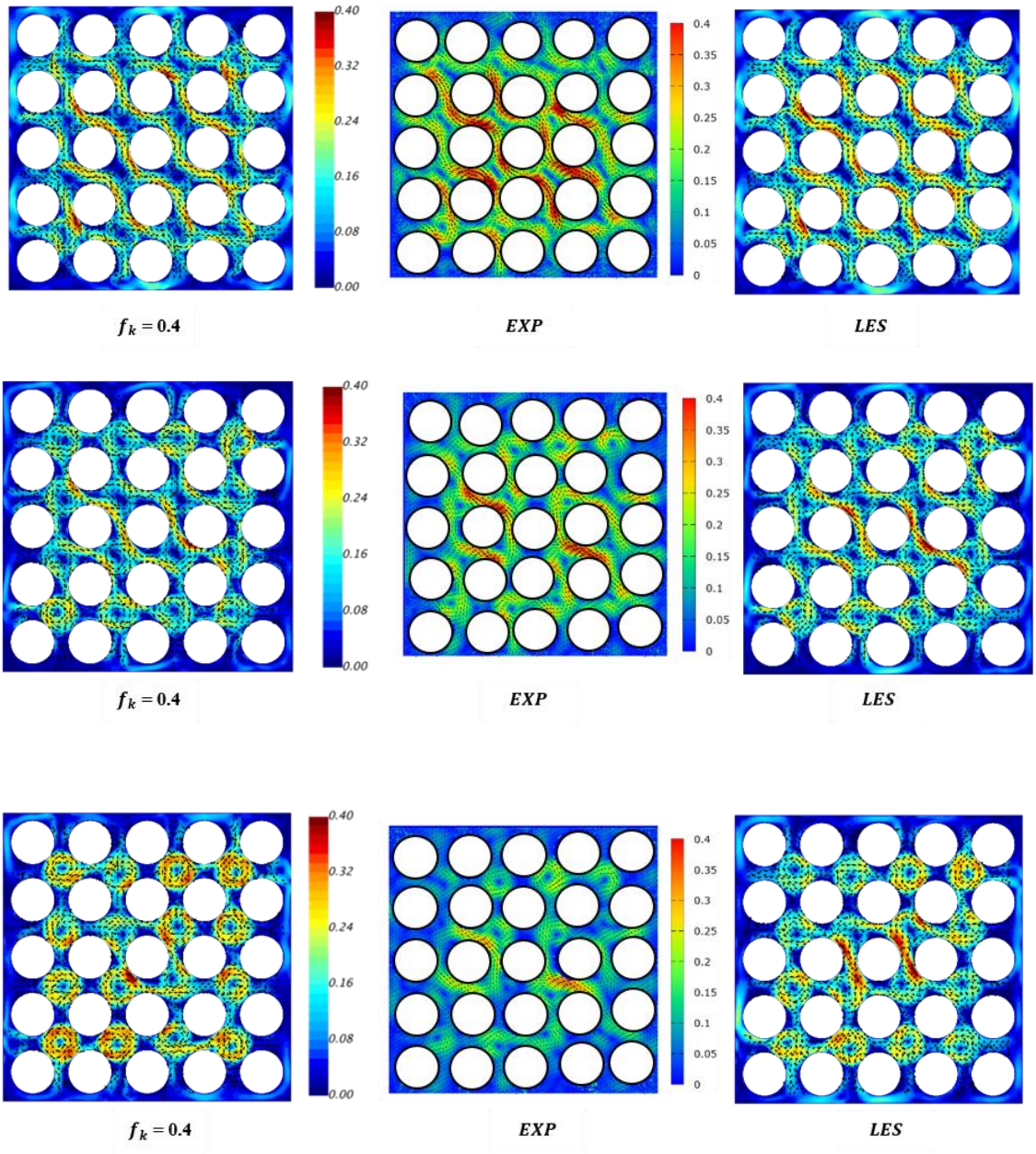

Figure 25 Velocity vector fields at the horizontal planes. y =5Dh (top). y =10Dh (middle). y =25Dh (bottom).

6.1.3. Spatio-Temporal Turbulent Flow Structure

Based on our analysis thus far, we observed that that the PANS model has a natural tendency to produce results similar to those for LES. In addition, we observed that the PANS models with the larger filters ($f_k = 0.6, f_k = 0.8$) tend to resolve the largest turbulent scales at the very end of the region downstream of the spacer grid (Figure 4). By using a different set of PANS filters, we can place the energy-based cut-off filter f_k at different intervals within the turbulent kinetic energy spectrum. Larger PANS filters will enable us to resolve only the largest turbulent scales in the computational domain in both space and time. The following section explores further the model to model comparison between the PANS and LES approach. However, it is important to note that further and in-depth studies on sensitivity analysis of resolved turbulent length and time scales versus PANS filters should be considered.

6.1.3.1. Temporal Analysis

We begin the temporal analysis of the resolved turbulent flow structure for the PANS and LES models by applying a time autocorrelation operator in order to evaluate the resolved turbulent time scales.

We present the normalized autocorrelation profiles of the streamwise fluctuating velocity component V_y' (Figure 27) along with the estimated integral time scales of the largest resolved eddies (Figure 28).

The time scales have been normalized by the time t_0 derived from hydraulic diameter D_h and average velocity in the fuel bundle V_0.

We present the main findings of this analysis, particularly in the region downstream of the spacer grid ($y = 20D_h$), where the fluid flow tends to reorganize itself and recovers into a fully developed flow structure as in the region upstream of the spacer grid. This is the region where we observed the initial resolution (liberation of the largest turbulent scales) for the PANS model with the largest filter.

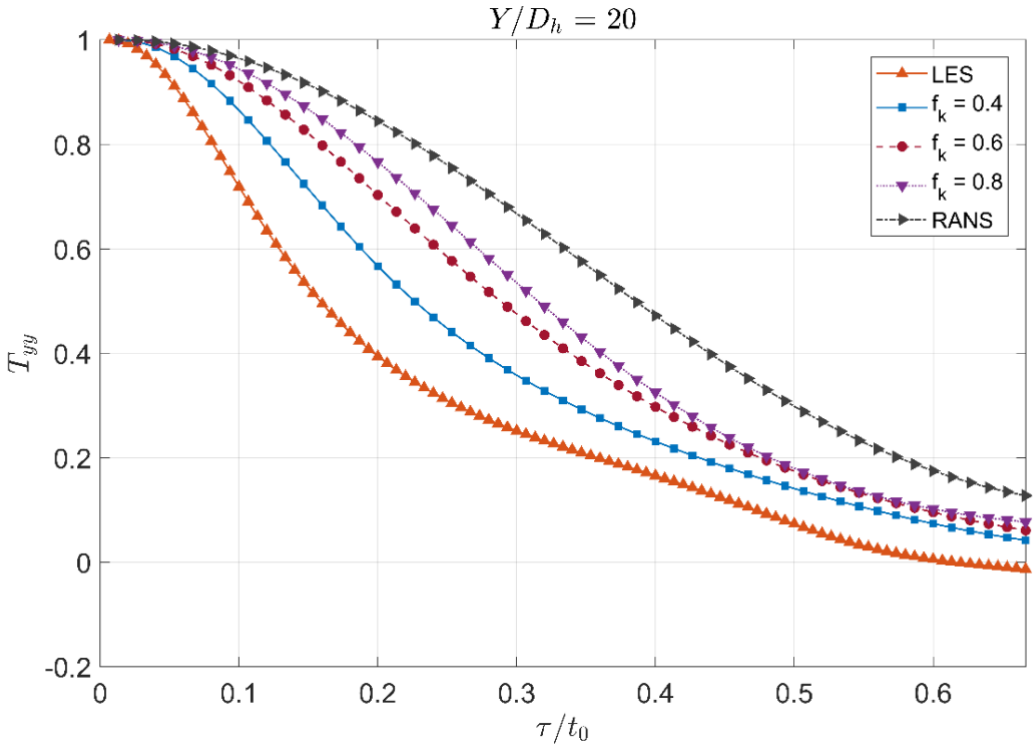

Figure 26 Normalized autocorrelation profiles of the streamwise fluctuating velocity component Vy'.

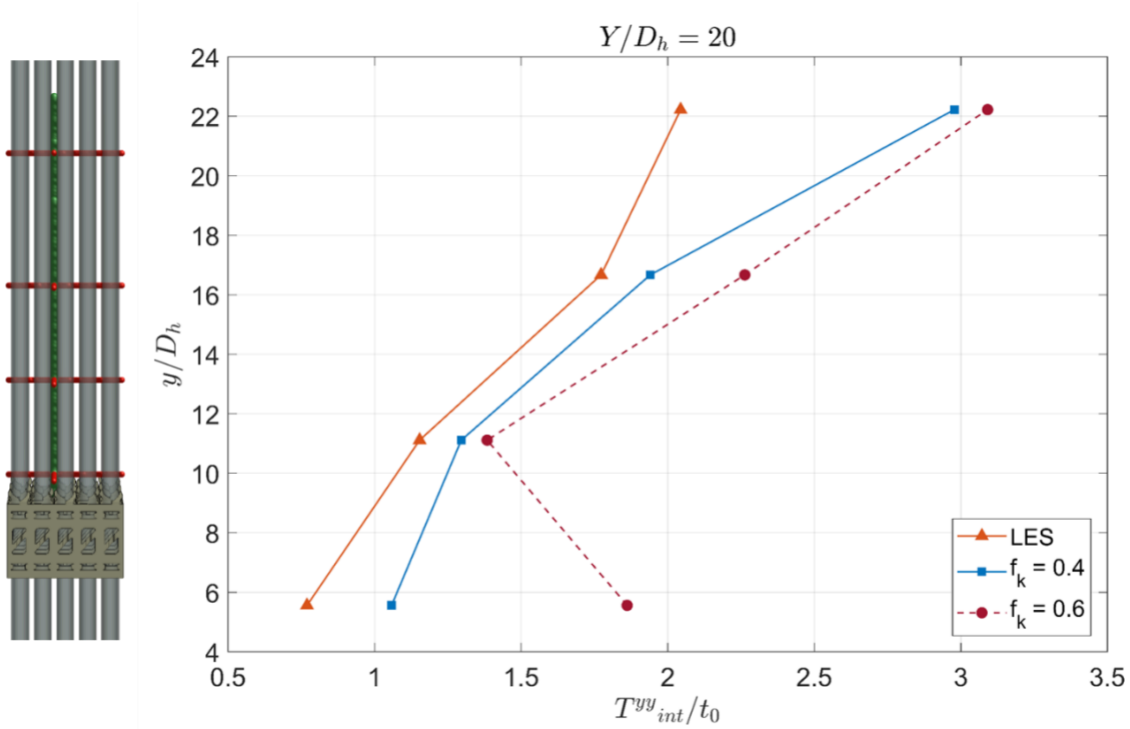

Figure 27 Integral time scales evaluated at four different locations downstream of the spacer grid.

Indeed, the temporal resolution of the turbulent length scales for the PANS model tends to approach that of the LES model as the PANS filter becomes smaller, as expected. Physical interpretation of these results shows an important trend that we have noticed during the secondary flow analysis.

We observed that as long as the turbulent eddies move downstream of the spacer grid, the turbulent eddies decelerate (larger integral time scales) along with the swirl motion of the vortices generated by the mixing vanes. It is also apparent from Figure 28 that for $f_k = 0.6$, the integral time scales in the region within vicinity of the mixing vanes are larger compared to those for the other two cases ($f_k = 0.4$ and LES).

This can be explained by examining Figure 7, where it can be observed that for the PANS model with the largest filters ($f_k = 1.0,\ f_k = 0.8,\ f_k = 0.6$), the fluid flow close to the spacer grid remains in a quasi-steady RANS-like state, which leads to larger integral time scales.

6.1.3.2. Spatial Analysis

The results obtained from the secondary flow analysis also suggest that not only the integral time scales increase downstream of the mixing vanes, but also the turbulent length scales. In order to test the modeling capability of the PANS models, we performed a two-point correlation analysis of the time signals for the fluctuating velocity components $V_i^{'}$. It shall be noted that the spatial analysis was performed at the same locations along the fuel rod bundle configuration as those for the temporal analysis.

Figure 29 shows the two-point correlation profiles of the streamwise fluctuating velocity component V_y', which were extracted from the region downstream of the spacer grid ($y = 20D_h$).

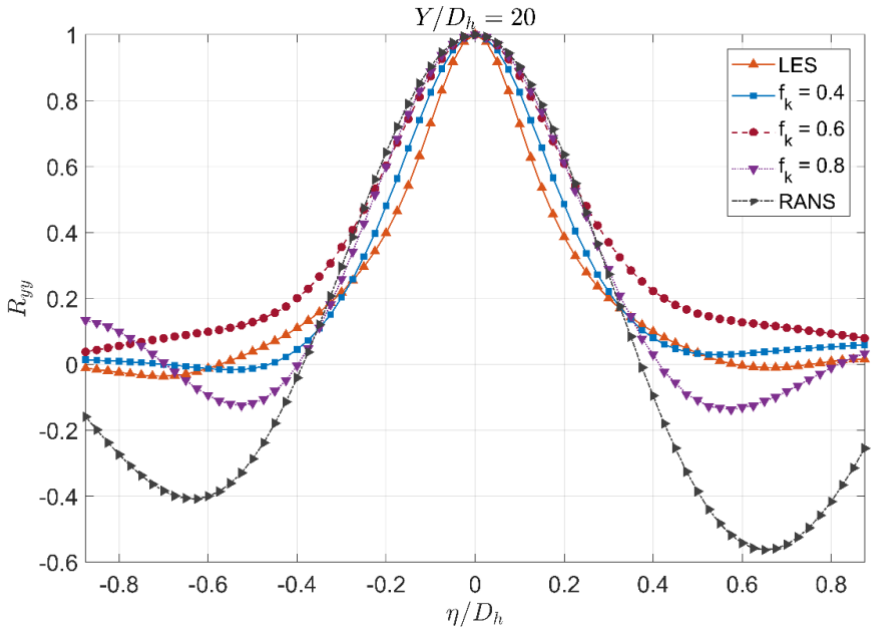

Figure 28 Two-point correlation profiles of the streamwise fluctuating velocity component Vy'.

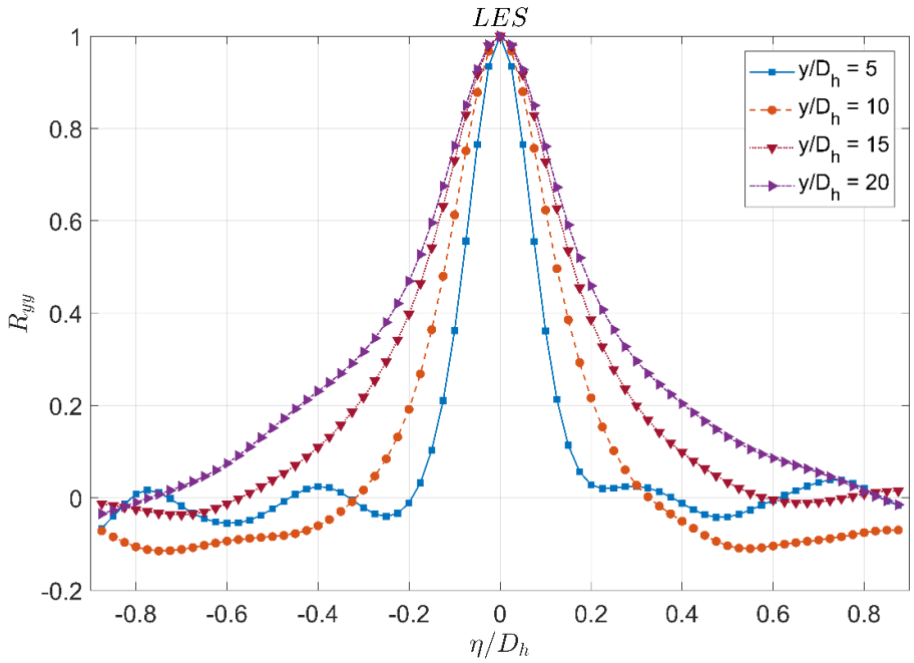

Figure 29 Two-point correlation profiles of the streamwise fluctuating velocity component Vy' obtained from the LES model at four different locations downstream of the spacer grid.

In general, the trend is the same as before, where the PANS model tends to produce results similar to those for the LES model as the PANS filter f_k becomes smaller.

We also plotted the two-point correlation profiles of the streamwise fluctuating velocity component V_y' obtained from LES at four locations downstream of the spacer grid, as shown in Figure 30.

It can be seen here that the two-point correlation profiles become wider at locations farther downstream of the spacer grid, which conforms well with the observed behavior of the instantaneous scalar velocity fields in Figure 7.

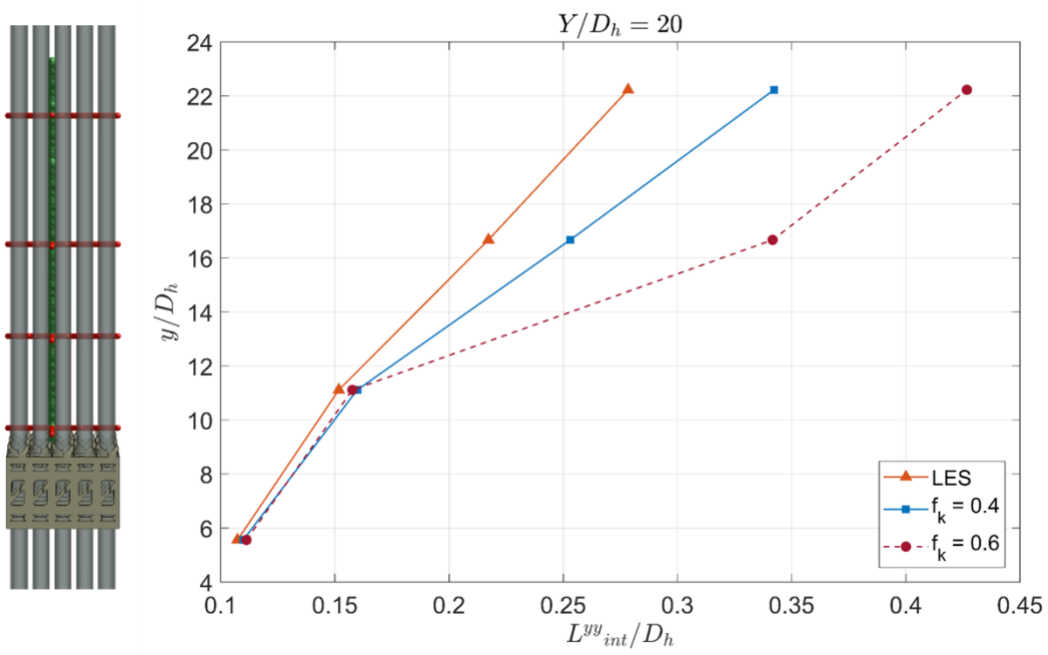

Figure 30 Integral length scales evaluated at four different locations downstream of the spacer grid.

The estimated integral length scales (Figure 31) offer deeper insight on how the PANS bridging model resolve the scales in the turbulent kinetic energy spectrum.

Based on the results obtained from spatial analysis of the turbulent flow structure, it is evident that the turbulent length scales become larger at locations farther downstream of the spacer grid. The rotating vortices generated by the mixing vanes become larger as they lose energy at locations farther downstream of the mixing vanes.

The two-point correlation analysis also shows that the turbulent flow structures downstream of the mixing vanes are primarily non-isotropic.

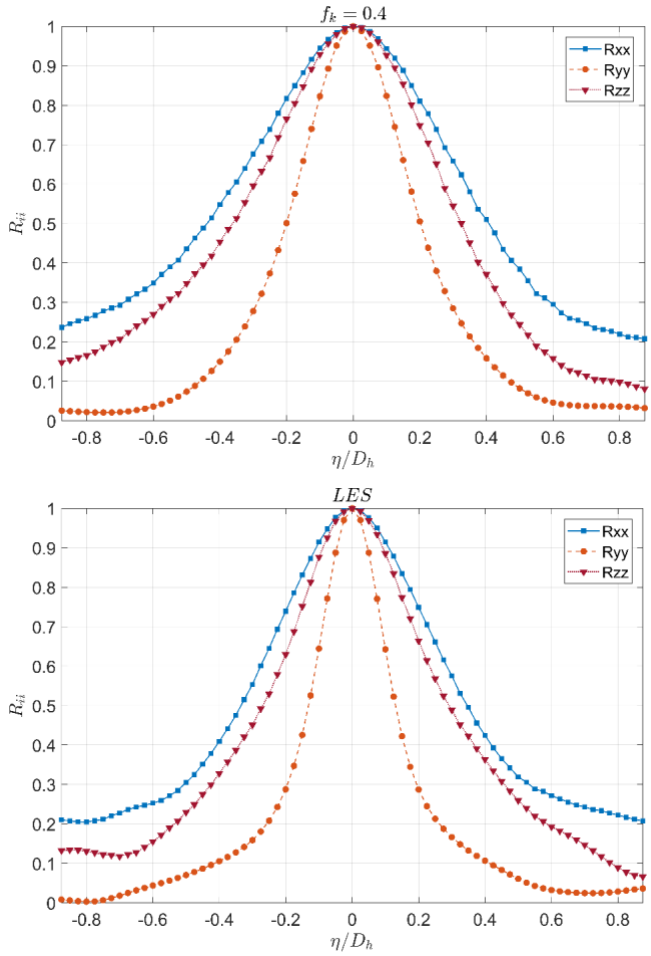

Figure 31 Two-point correlation profiles of the three fluctuating velocity components at y=20Dh. LES results (top). PANS results with fk=0.4 (bottom).

Figure 32 shows the two-point correlation profiles of the three fluctuating velocity components obtained from the PANS model with the smallest filter ($f_k = 0.4$) and LES model.

It can be seen that the turbulent length scales of the two lateral components of the fluctuating velocity field ($V_x^{'}$, $V_z^{'}$) are certainly larger than those for the vertical component ($V_y^{'}$).

This indicates that the turbulent flow structures are wider in the horizontal direction. This behavior is captured by both the LES and PANS models.

6.1.3.3. Spectral analysis

In order to present the spatio-temporal results of the turbulent flow structure in a better way, we conducted spatio-temporal spectral analysis of the turbulent flow structure and we present the results in terms of the frequency ω and wave number κ.

The analysis was carried out in the region downstream of the spacer grid ($y = 20D_h$), as shown in Figure 33, where the flow tends to recover to its fully developed structure and the flow is less influenced by the presence of the spacer grid.

We normalized all of the spectra based on the largest space and time scales in order to demonstrate the cut-off action of the LES and PANS models within the inertial turbulent scale range.

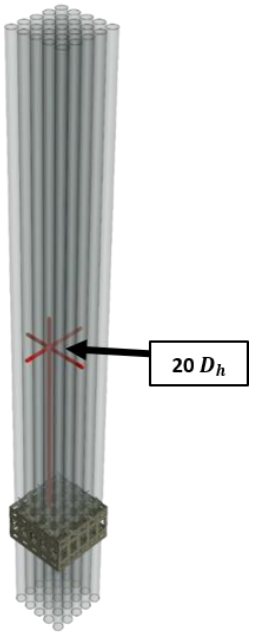

Figure 32: Location downstream of the spacer grid for spatio-temporal spectral analysis of the fluctuating velocity components.

We investigated the fluctuating velocity signals in the frequency domain by performing Fourier transform of the fluctuating velocity components $V_i^{'}$. The results obtained from the temporal analysis can be better represented in the frequency domain (i.e., turbulent frequency spectra).

Figure 34 shows the turbulent frequency spectra of the vertical fluctuating velocity component $V_y^{'}$, where the frequency range is normalized with respect to the largest frequency of the spectrum.

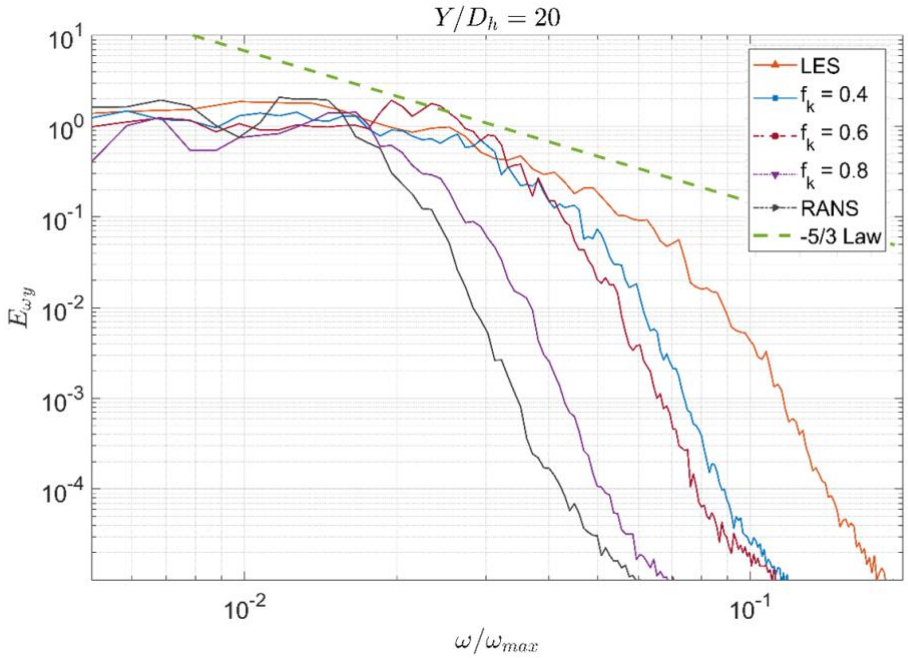

Figure 33 Turbulent frequency spectra of the streamwise fluctuating velocity component Vy'

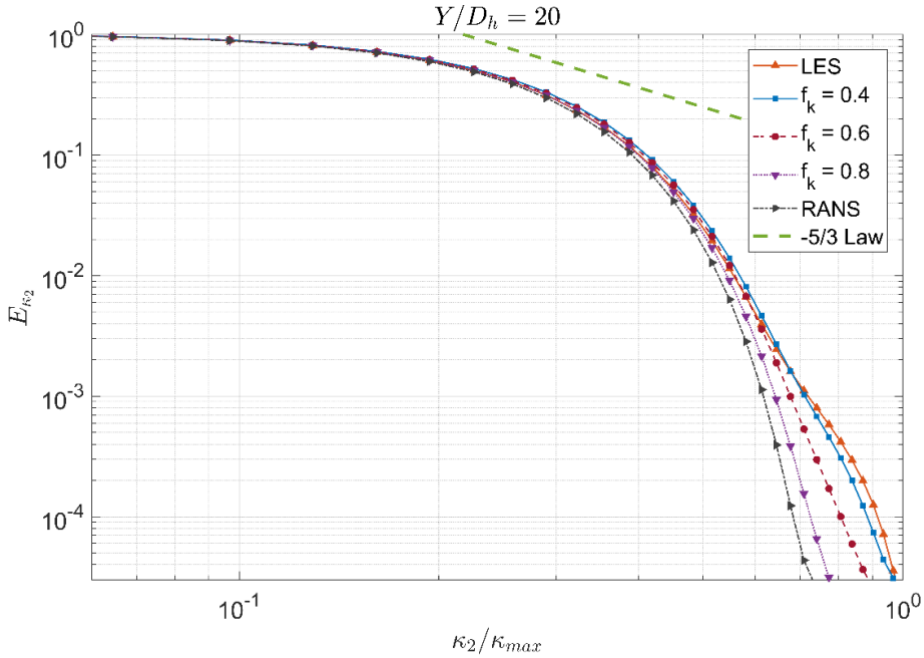

Figure 34 Turbulent energy spectra of the streamwise fluctuating velocity component Vy'.

It can be seen that the frequency cut-off of the time signal increases as the PANS filter f_k become smaller, which increases the fraction of the filtered flow field. The presence of a low Reynolds number flow is also evident when we observe a small fraction of the turbulent frequency spectra with a slope of -5/3, which is characteristic of the inertial subrange.

The same cut-off behavior can be observed in the turbulent energy spectra $E_i(\kappa)$ of the streamwise fluctuating velocity component V_y' which are plotted as a function of the wave number κ, as shown in Figure 35.

We obtained the turbulent energy spectra $E_i(\kappa)$ by performing Fourier transform of the normalized two-point correlation analysis, where the wave number is normalized with respect to the largest wave number κ_{max} of the spectrum.

These results show the modeling capability of the PANS models, where the desired spatio-temporal resolution of the turbulent flow can be imposed by varying the unresolved-to-total turbulent kinetic energy filter f_k.

6.2. Invariant Analysis with Nek5000

6.2.1. Flow Field Analysis and Validation

The comparison with PIV experimental data has been done on two vertical planes, the first in the near wall region and the second in the interior part of the computational domain. Those planes are labeled as plane 1 and plane 2 in Figure 1.

In the following are presented three non-dimensional time-averaged velocity components and root mean square profiles at a distance of two hydraulic diameters downstream the spacer grid. On Figure 36 and Figure 37 we present a comparison between the Nek5000 results for two local polynomial order, respectively *N=6* and *N=8*, the experimental PIV results and results from previous LES simulations performed with the finite volume code Star-CCM+.

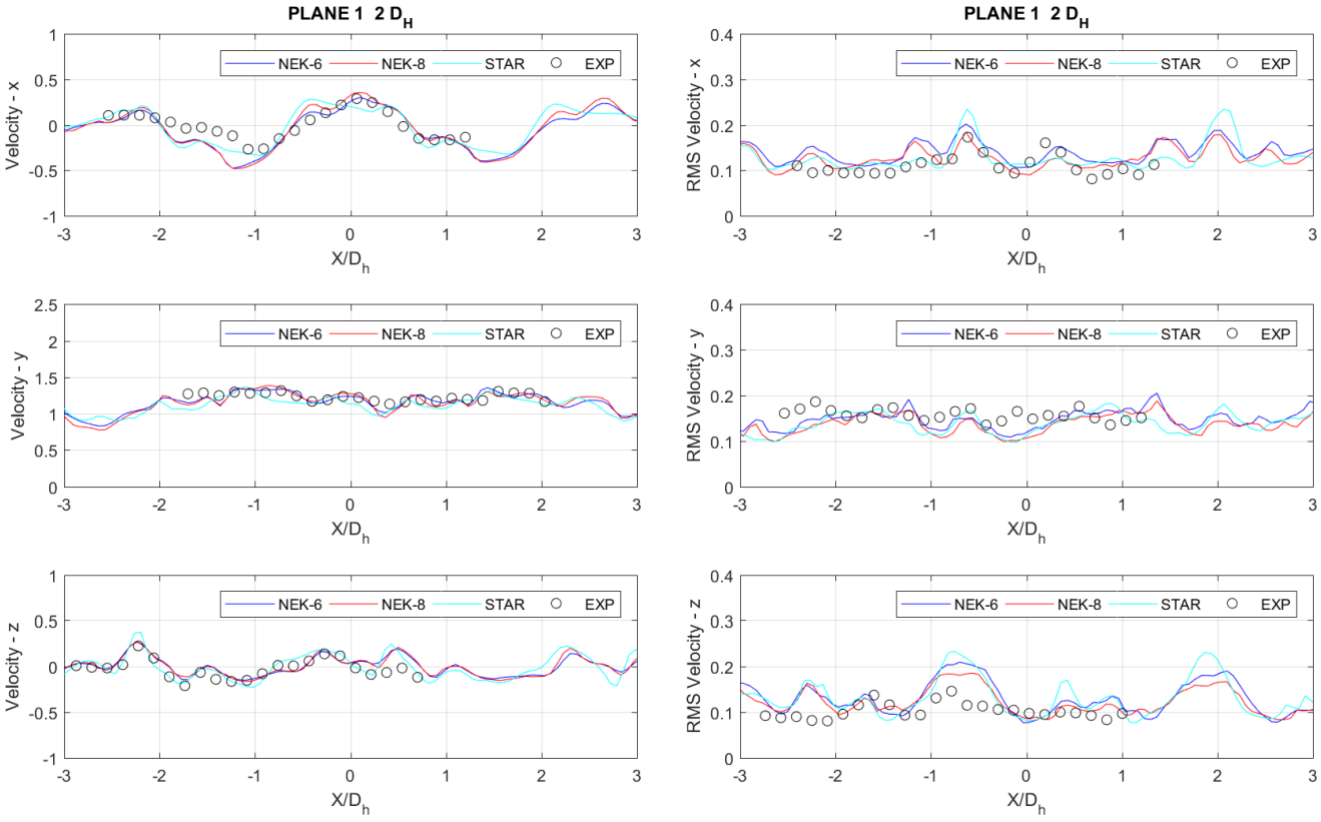

Figure 35 Non-dimensional velocity and RMS on Plane 1.

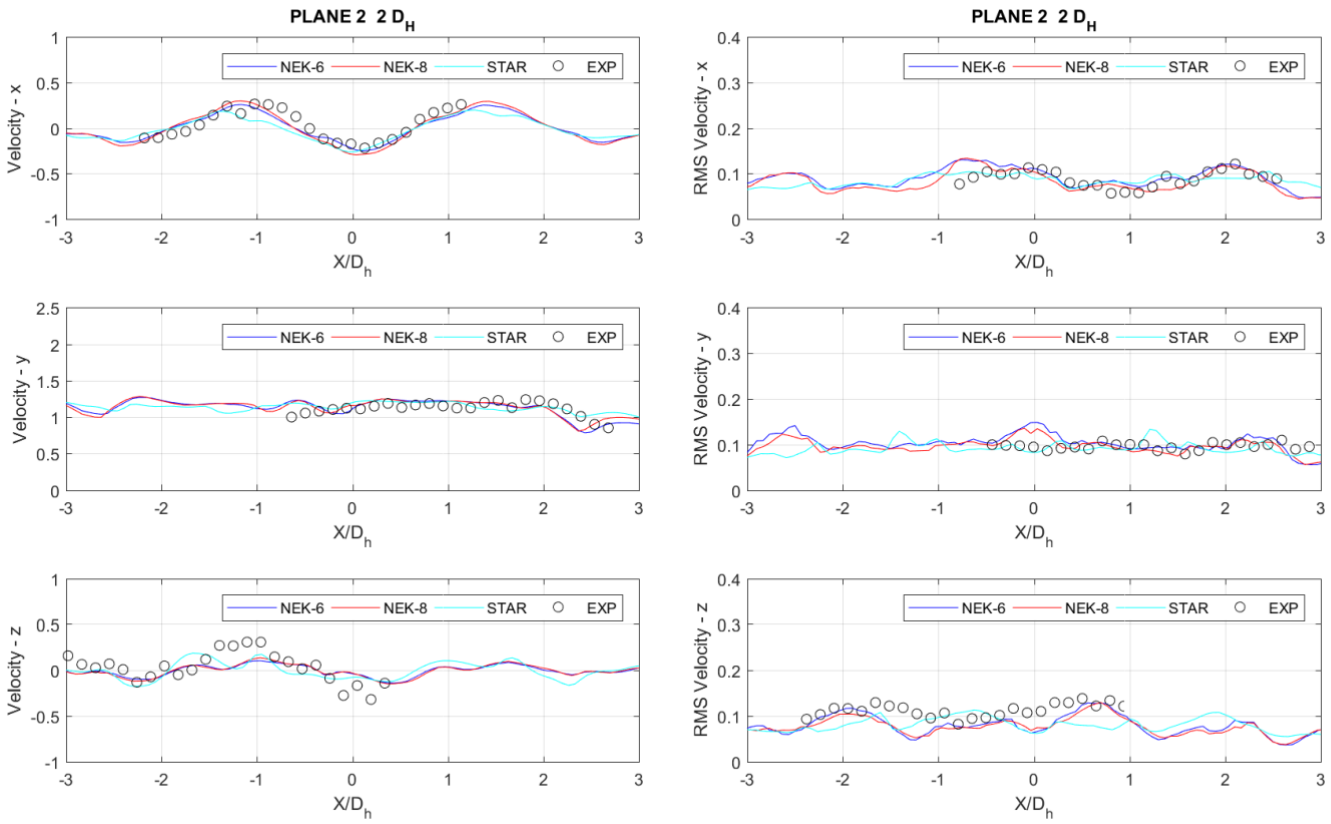

Figure 36 Non-dimensional velocity and RMS on Plane 2

The comparison between the two SEM polynomial orders indicates that the spectral elements solution is converged and that $N=6$ is sufficient to capture the flow physics at such moderate Reynolds number.

The comparison with the Star-CCM+ LES solution indicates a good agreement between Nek5000 and Star-CCM+ results. This is especially true for the time averaged velocity components profiles. The RMS comparison shows some differences between the two models/numerical approaches, but still consistent. Small differences are noticed in the RMS peaks magnitudes, but their location is fully captured.

The comparison with experimental data gives very good results for the first order statistics comparison, but not fully satisfactory in term of RMS velocities. Some of the peaks in the simulation are not captured in the experiment. This can be due to the lack of time convergence on the experimental side, geometrical differences between the simulation geometry and the real spacer grid geometry and boundary conditions.

Overall the comparison with experimental data is consistent if not better than previous simulation efforts and it is judged sufficient to use this simulation data for further deepen our understanding of the flow physics in this class of flows. Numerical results gave insight to the vanes induced secondary flow structure.

6.2.2. Reynolds stress tensor components

The analysis has been performed for each sub-channel. In the following we will focus mainly on two central sub-channels which differs mainly on the vane orientation. The vane structure results rotated by 90^0 with respect to the streamwise (y-direction).

Results are presented for three different elevations ($y/D_h = 1$, $y/D_h = 10$, $y/D_h = \infty$) in the downstream region of the spacer grid. In order to take into account the fully developed flow condition in the downstream region of the grid, we also presented results from the inlet recirculation flow region ($y/Dh = \infty$). As we move downstream the vanes induced secondary flow structure starts to decay.

Figures 38 and 39 show the contour plots of the six Reynolds stresses components in the downstream region.

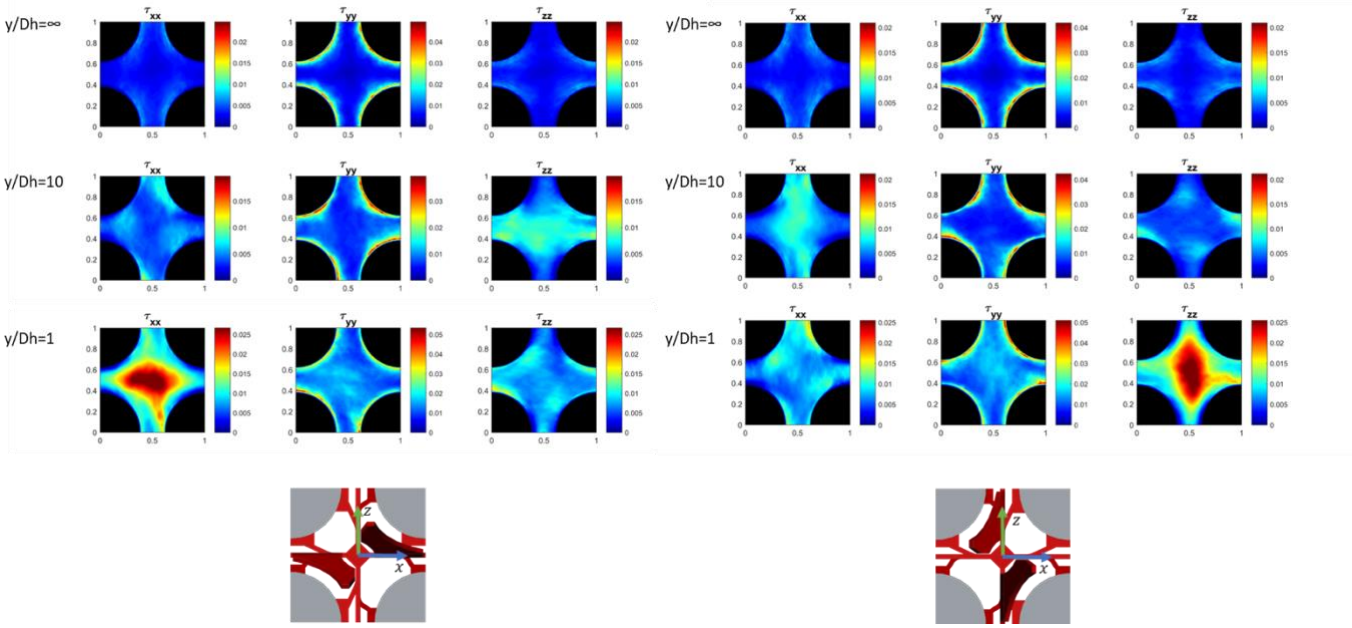

Figure 37 Normal components of the Reynolds stress tensor. X-splitted vanes (left). Z-splitted vans (right).

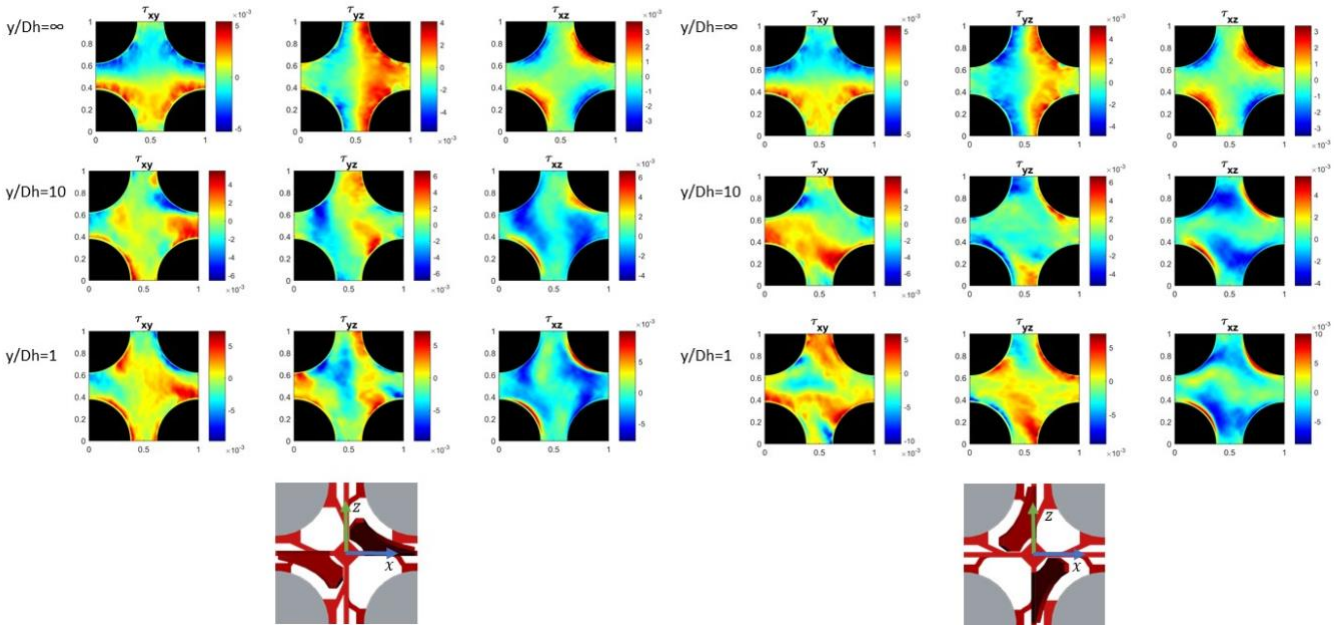

Figure 38 Shear components of the Reynolds stress tensor. X-splitted vanes (left). Z-splitted vanes (right)

A symmetry in the normal stresses components is present for the in-plane energy components τ_{xx} and τ_{zz}. The two components results are equal but rotated by 90 degrees, reflecting the vanes geometrical configuration.

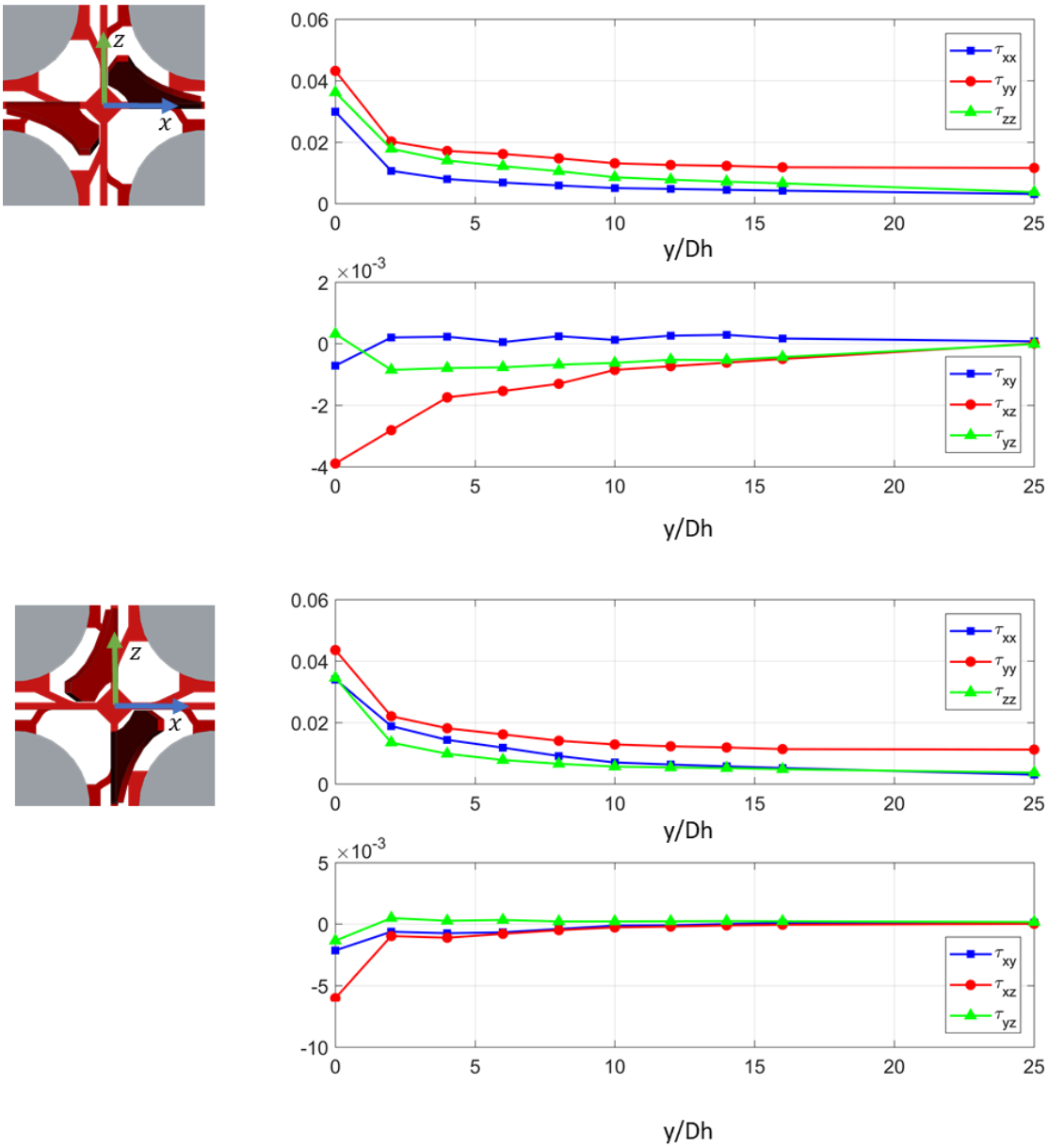

Figure 39 Non-dimensional sub-channel average Reynolds stresses evolution in the downstream region of the vanes. X-splitted vanes (top). Z-splitted vanes (bottom).

The Reynolds stress tensor components, which are averaged over the entire sub-channel, tend to redistribute themselves. Figure 40 presents the downstream profiles of the six averaged components of the Reynolds stresses.

In the figure the fully developed flow condition is represented at y/Dh = 25. In the region close to the vanes we observe a peak in the normal components τ_{ii}, and depending on the vane orientation we observe:

- For z-direction splitting vanes: the corresponding normal stress in the z-direction τ_{zz} prevails over the x-direction normal component τ_{xx}. On average the off diagonal elements (shear stress τ_{ij}) decay faster in the downstream region.

- For x-direction splitting vanes: the corresponding normal stress in the x-direction τ_{xx} prevails over the z-direction normal component τ_{zz}. There is a slower decay of the shear stresses τ_{ij} in the downstream region.

Figure 41 reports a three-dimensional representation of the Reynolds stresses normal components τ_{ii}. After the spacer grid the corresponding normal energy corresponding to the vane orientation (x direction/z direction splitting) prevails in the center of the sub-channel. As the flow moves downstream the shear stresses components τ_{ij} of the Reynolds stress tensor tend to zero. The streamwise Reynolds stress diagonal component τ_{yy} become dominant with respect to the other two $\tau_{xx}\ and\ \tau_{zz}$. The subchannel averaged components of the Reynolds stress tensor are such that the tensor, representing such an averaged state, tends to naturally diagonalize itself, with a rod-like state of turbulence, one large dominant diagonal component ($\tau_{yy} > \tau_{xx}$, $\tau_{yy} > \tau_{zz}$).

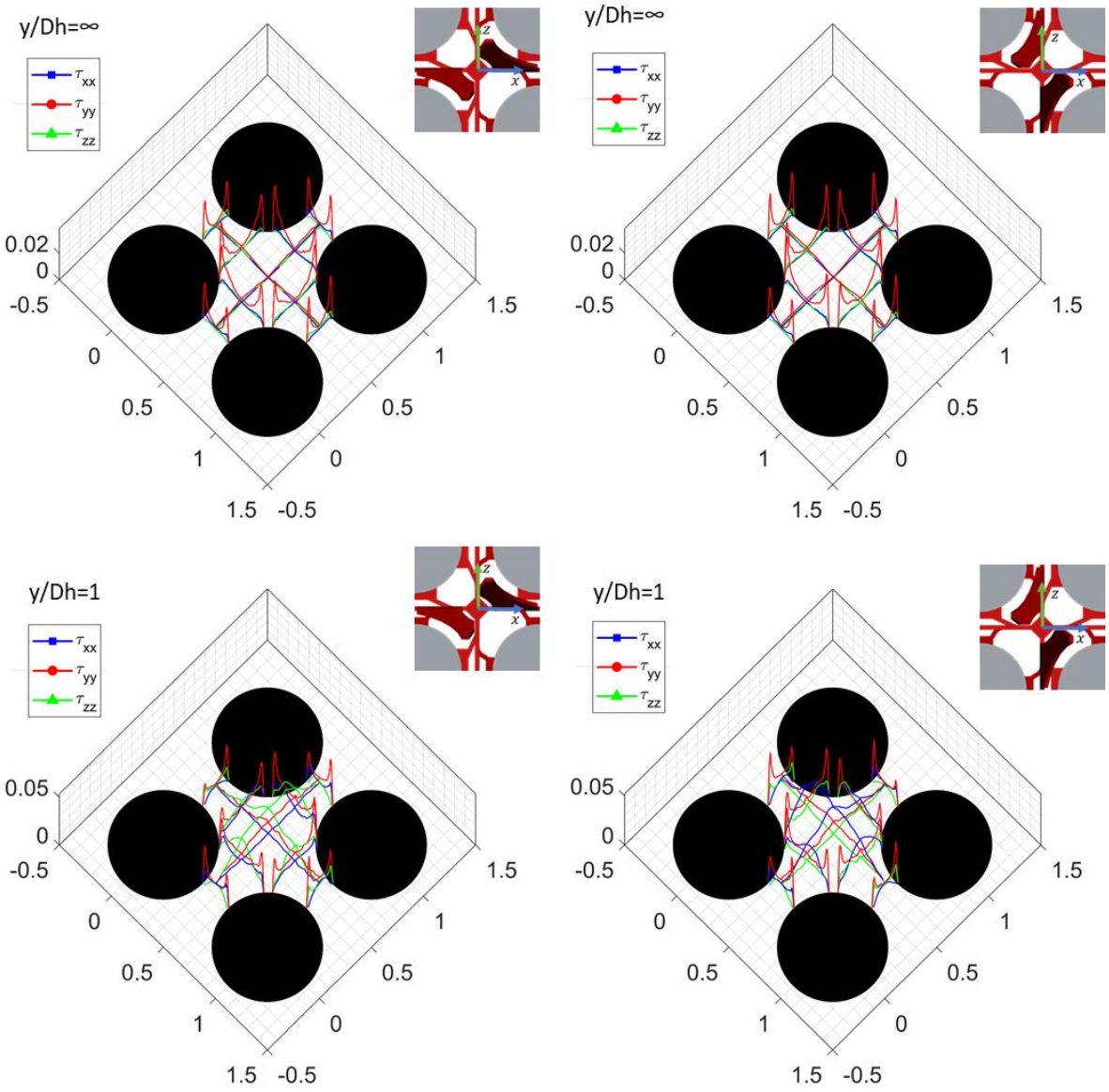

Figure 40 Normal Reynolds stress sub-channel distribution

6.2.3. Lumley invariant analysis

We started our analysis with the evaluation of the Reynolds stress anisotropic tensor invariants in the flow fully developed region, where the spacer grid has no effect. The two invariants have been evaluated along two lines. The first line goes along the wide gap of the sub-channel. The second line goes along the narrow gap of the sub-channel.

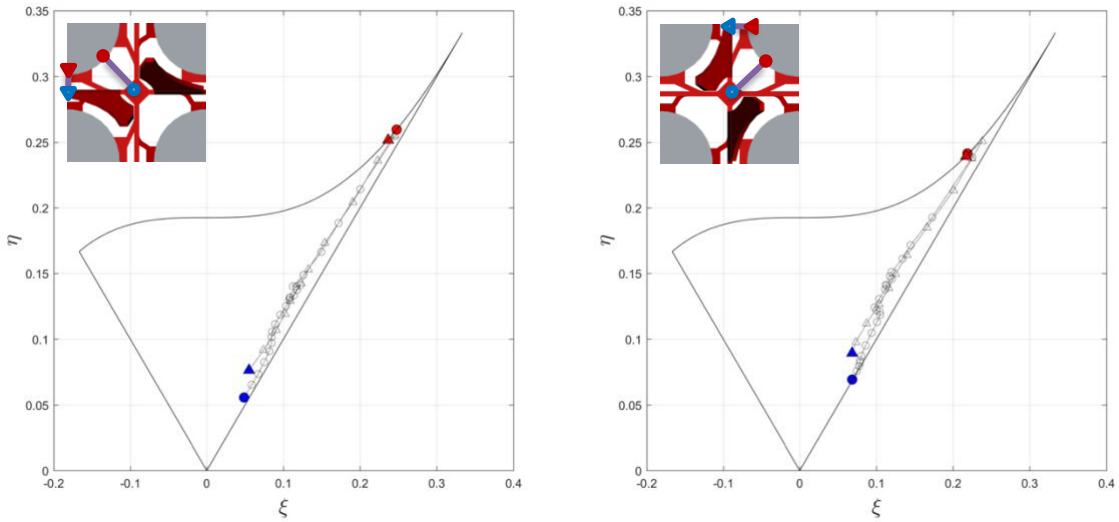

Figure 41 Lumley states in the fully developed region. Narrow gap (triangles). Wide gap (circles). Wall region (red), center of the gap (blue).

Figure 42 presents the results for two central sub-channels and the geometrical location of the two lines. In the wide-gap region we observe the typical channel flow behavior (wall turbulence). Near the wall, the normal velocity component becomes negligible and the turbulence is mainly two-dimensional. As we move towards the center

of the wide gap region, the turbulent state is axisymmetric and tends to be nearly isotropic in the center of the sub-channel.

A very similar behavior is observed for the narrow gap profile in the near wall region. The only difference is that in the wide gap case the turbulent state collapses on the right side of the Lumley triangle (purely axisymmetric turbulent state), whereas it doesn't in the narrow gap case.

The results are in agreement with the experimental findings of (Don and Tavoularis, 2018) for the bare rod-bundle case at a *Re = 100,000* and *P/D = 1.149*, and with LES simulation results of (Merzari and Ninokata, 2011) for the bare rod-bundle case at *Re = 5500* and *Re=6400* with *P/D = 1.05*.

In the latter case, thanks to a very small *P/D* ratio, the differences in the turbulent structure, between the narrow and wide gap were more noticeable. The analysis showed a shift from purely two-components axisymmetric turbulence at low-Reynolds number to a condition consistent with the typical behavior of wall turbulence for higher Reynolds number inside the narrow gap region.

The present study expands the analysis of (Merzari and Ninokata, 2011) to a larger P/D ratio (P/D = 1.32) and a larger Reynolds number (Re = 14.000). As expected, in such conditions, the differences in the wall turbulent structure of the wide and narrow channel are minimal.

In order to have an overall picture of the turbulent state of the Reynolds stress anisotropic tensor inside the entire sub-channel region, we plot in Figure 43 the state of the two differently oriented sub-channel vanes at different elevations.

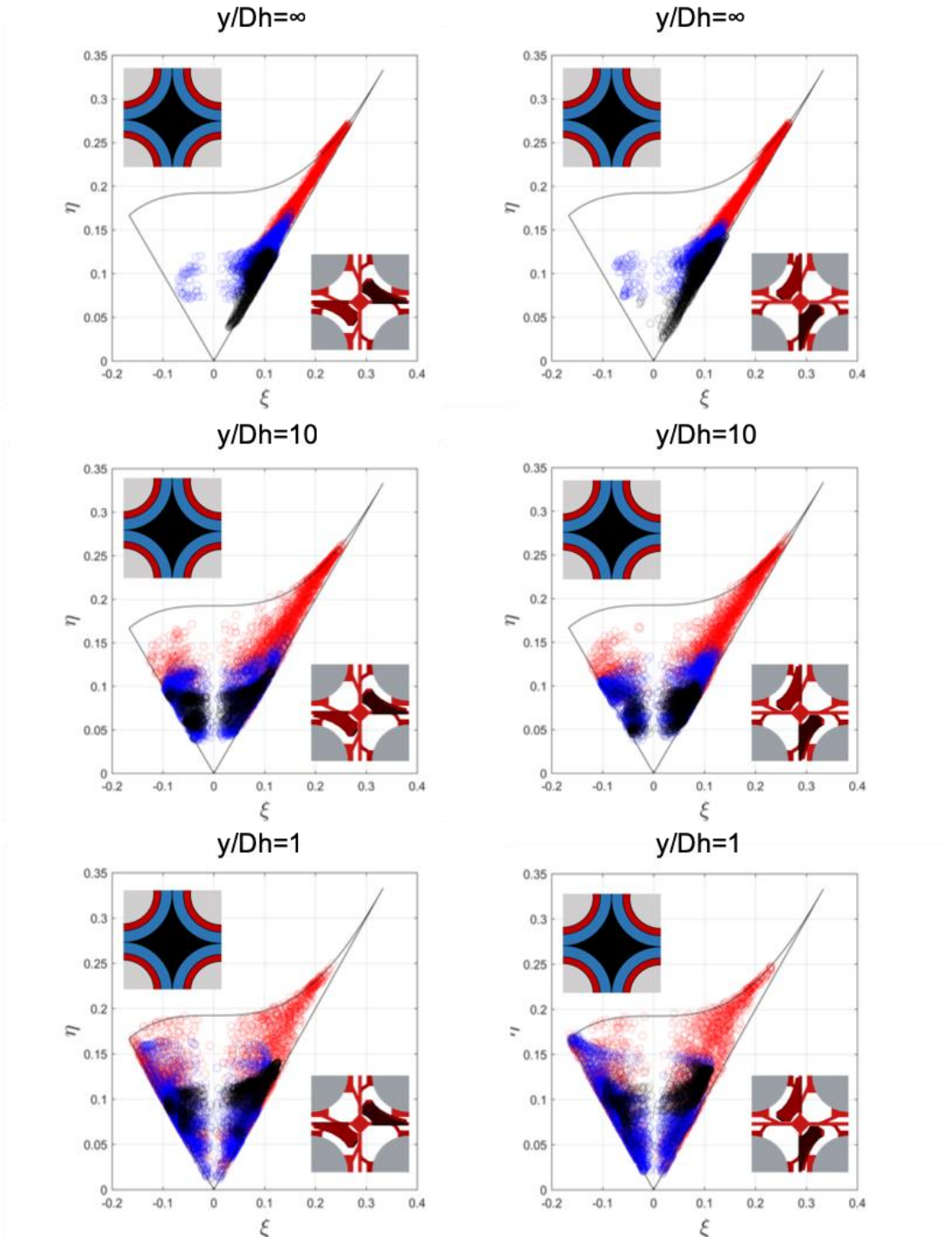

Figure 42 Distribution of the Reynolds stresses anisotropic states. Wall (red). Intermediate (blue). Core (black)

A distinction has been made between the inner rod bundle wall region (red), an intermediate region (blue) and the central region of the sub-channel (black). In the region close to the mixing vanes (*y/Dh = 1*) the turbulent state is characterized by rod-like and disk-like turbulence. In the wall region the points fall in the upper region of the triangle, limited by the 2 components turbulent state. In the intermediate and core region of the sub-channel the points occupy the lower part of the triangle, with states that extend down to isotropic region.

In the region far from the spacer grid (*y/Dh=10*) the general trend is a shift from the disk-like turbulence to rod-like turbulence, despite the fact that the typical wall behavior is observed at every height. In fact most of the points in the near-wall region extends from the 2 component turbulence, down along the disk-like turbulent state with $\xi > 0$. As we move far from the wall the points in the core-region tend to the isotropic state along the rod-like turbulence line.

Finally, in the fully developed region (*y/Dh* = ∞) the majority of the points spread along the rod-like turbulence line. As we move away from the wall the points tend to approach the isotropic state as expected. The same trends can be observed for both vane-oriented sub-channels.

In order to have an overall picture of the turbulent state we averaged the sub-channel Reynolds stress anisotropic states at different elevations downstream the vane region.

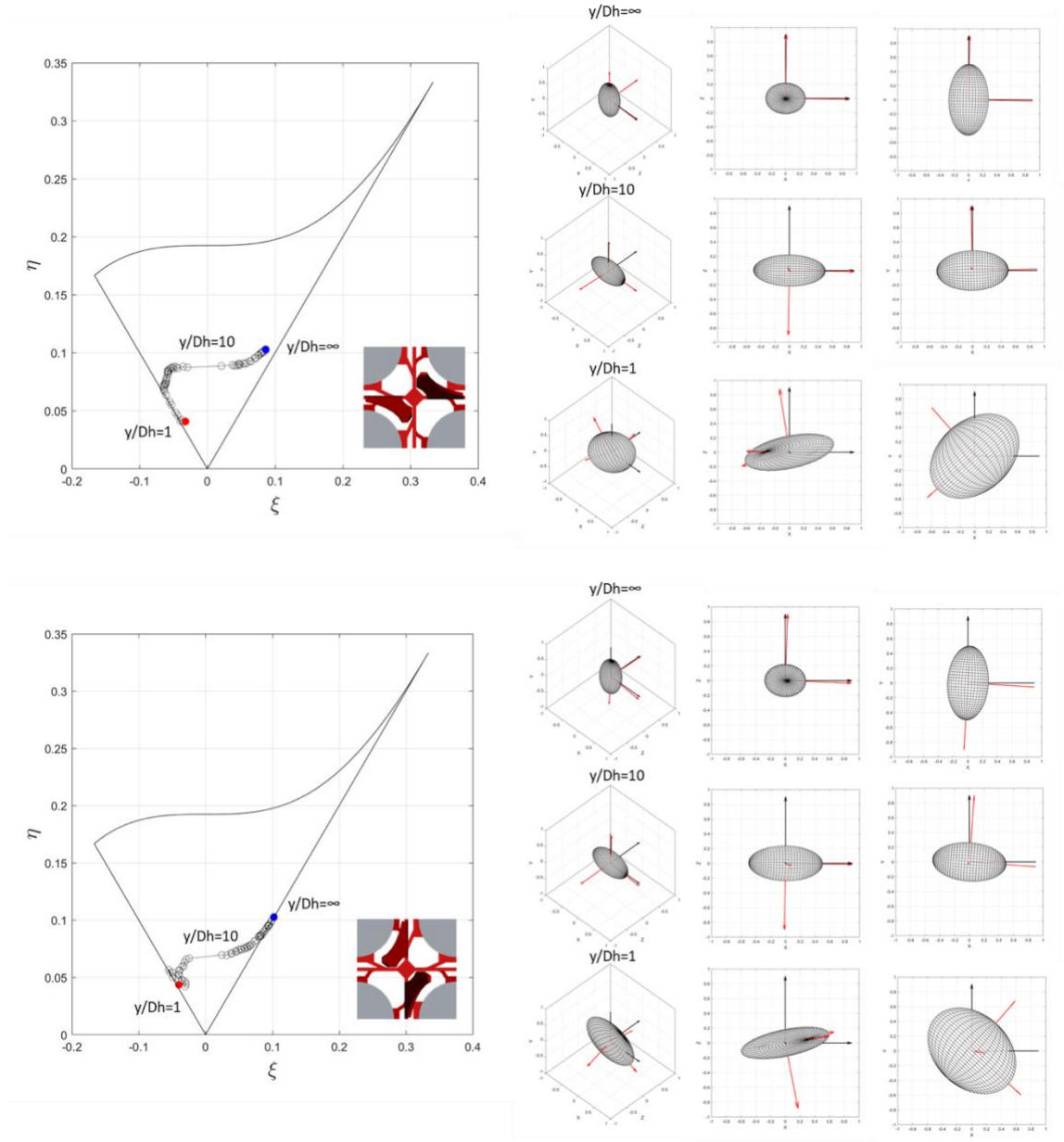

Figure 43 Sub-channel averaged turbulent state. Energy ellipsoids. Reference frames: computation (black), principal axes (red).

In Figure 44 we see that as we move downstream the spacer grid the average turbulent state shifts from disk-like turbulence to rod-like turbulence.

As the flow reaches the vanes, it receives a twist, and spreads at the same time in the span-wise direction.

This increase the two eigenvalues (energies) corresponding to the horizontal direction (*x-z plane*). As it moves downstream it reorganize itself where the energy increase in the span-wise direction *y*.

The two eigenvalues corresponding to the horizontal direction (*x-z*) decrease. Additionally it has been shown previously that as the flow moves downstream reorganize its averaged Reynolds stress state, such that its anisotropic components tends to zero and it tends to be diagonal. As we showed the dominant diagonal component is the normal one τ_{yy}.

In Figure 44 the turbulent energy ellipsoid corresponding the sub-channel averaged turbulent state is also represented. In its representation the ellipsoid is in its principal coordinate system (red). The system is represented with respect to the original coordinate system (black). The shape of the ellipsoid is the same for both sub-channels.

The principal coordinate system associated to the turbulent state has a different, but symmetric, orientation. The tendency for the principal coordinate system is to change its orientation in the downstream region. As we move downstream, the principal axis tend to be aligned with the Eulerian reference frame.

The difference between the two subchannels is the orientation between the principal coordinate system and the local (Eulerian) coordinate system. For example, in the fully developed region ($y/Dh = \infty$), the principal axis corresponding to the largest

eigenvalue (*y-direction*) has opposite direction for the *z-splitted* and *x-splitted* oriented vanes.

The tendency of the principal axis to be aligned to the Eulerian reference frame is due to the fact that the subchannel averaged shear stresses of the Reynolds stress tensor tend to equilibrium.

The Reynolds stress anisotropic tensor has a tendency to reorganize itself in a diagonal matrix and the spectral space of the matrix tends to be aligned with the physical space of the simulation.

7. CONCLUSIONS

In this study, we have demonstrated the applicability of PANS bridging turbulent modeling paradigm to predict the complex turbulent flow structures in the region downstream of the spacer grid of a fuel rod bundle configuration.

By choosing the appropriate energy-based cut-off filter in the PANS model, one can directly impose the desired degree of resolution and resolve large turbulent scales at minimum computational cost.

The robust theory by which PANS is founded is directly a parent of RANS modeling, which is a well-known, tried-and-tested modeling approach for engineering applications. The model to model results show that the PANS tends to produce results similar to those from LES with reasonable agreement by using the appropriate cut-off filter. In addition, PANS modeling can be adopted in all types of commercial CFD codes with standard RANS models.

We have shown that PANS modeling acts on the closure coefficients of the selected RANS model. We have also analyzed the first and second-order turbulence statistics along with the spatio-temporal turbulent flow structures and the results show good agreement with the PANS paradigm. Since PANS closure model is decoupled from the computational grid, an internal consistency check should be performed.

The mesh resolution should be commensurate with the externally imposed PANS filter. This feature makes PANS models suitable for discretization error estimates, based on grid convergence studies like grid convergence index (GCI). We have also compared

the numerical results with PIV experimental data available in the scientific literature and we found that the LES model and PANS model with the smallest filter ($f_k = 0.4$) show good agreement with the PIV data. The introduction of validation metrics also confirmed the general observed trend, indicating that these models are capable of predicting the vortex-induced secondary flow structures with reasonable accuracy.

The turbulent flow structure identified by the application of the Reynolds stress invariant analysis has been applied for this work.

Data from wall-resolved large eddy simulation using the spectral element code Nek5000 has been used to perform the analysis.

The simulations have been conducted at two polynomial orders to verify the results and they have been compared against available PIV data. The results of comparisons are excellent at least for the first order statistics and are considered better or equal to previous simulation efforts and they are judged sufficient to be used to deepen our understanding of the flow physics in this class of flows. The results showed a reorganization of the Reynolds stresses components in the downstream region of the spacer grid.

On average the Reynolds stress tensor has a natural tendency to become diagonal in the fully developed region. The orientation of the vanes with respect to flow direction has its impact on the Reynolds stress tensor. A symmetric behavior between sub-channels has been observed. The turbulent structure has been analyzed using the Lumley's triangle approach.

The typical behavior of fully-developed channel flow turbulence has been observed at all heights: turbulence goes from a highly anisotropic state to near isotropy.

However, when averaging the state across regions of the sub-channels, we observe a trend from overall disk-like turbulence behavior (two dominant eigenvalues) in the region close to the vanes to rod-like turbulence behavior (one dominant eigenvalue) in the fully developed region.

This has been observed consistently across all sub-channels examined and it is consistent with the presence of the split vanes which impart near two-dimensional behavior on the flow.

The results provided in this work contribute to an invaluable resource to further refine RANS turbulence models in this geometry and they also have the potential to lead to a deeper understanding of the effect of the vanes and their optimization.

REFERENCES

Bieder, U., Falk, F., Fauchet, G., 2014. Progress in Nuclear Energy LES analysis of the fl ow in a simpli fi ed PWR assembly with mixing grid 75, 15–24. https://doi.org/10.1016/j.pnucene.2014.03.014

Busco, G., Hassan, Y.A., 2019. Solution verification of PANS model for a PWR fuel assembly. Nucl. Eng. Des. 353, 110213. https://doi.org/10.1016/J.NUCENGDES.2019.110213

Busco, G., Hassan, Y.A., 2018. International Journal of Heat and Fluid Flow Space and energy-based turbulent scale-resolving simulations of fl ow in a 5 × 5 nuclear reactor core fuel assembly with a spacer grid. Int. J. Heat Fluid Flow 71, 420–441. https://doi.org/10.1016/j.ijheatfluidflow.2018.04.003

Busco, G., Merzari, E., Hassan, Y.A., 2019. Invariant analysis of the Reynolds stress tensor for a nuclear fuel assembly with spacer grid and split type vanes. Int. J. Heat Fluid Flow 77, 144–156. https://doi.org/10.1016/J.IJHEATFLUIDFLOW.2019.04.006

CHOI, K.-S., LUMLEY, J.L., 2001. The return to isotropy of homogeneous turbulence. J. Fluid Mech. 436, 59–84. https://doi.org/10.1017/S002211200100386X

Deville, M.O., Fischer, P.F., Mund, E.H., 2002. High-Order Methods for Incompressible Fluid Flow. Cambridge University Press, Cambridge. https://doi.org/10.1017/CBO9780511546792

Don, A., Tavoularis, S., 2018. Measurements of turbulent flow in a large-scale model of

a 37-rod bundle. Nucl. Eng. Des. 337, 116–127. https://doi.org/10.1016/J.NUCENGDES.2018.06.018

Fischer, P., Mullen, J., 2001. Filter-based stabilization of spectral element methods. Comptes Rendus l'Académie des Sci. - Ser. I - Math. 332, 265–270. https://doi.org/10.1016/S0764-4442(00)01763-8

Germano, M., 1992. Turbulence: the filtering approach. J. Fluid Mech. 238, 325–336. https://doi.org/10.1017/S0022112092001733

Girimaji, S.S., 2006. Partially-Averaged Navier-Stokes Model for Turbulence: A Reynolds-Averaged Navier-Stokes to Direct Numerical Simulation Bridging Method. J. Appl. Mech. 73, 413. https://doi.org/10.1115/1.2151207

Kang, S.K., Hassan, Y.A., 2016. Computational fluid dynamics (CFD) round robin benchmark for a pressurized water reactor (PWR) rod bundle. Nucl. Eng. Des. 301, 204–231. https://doi.org/10.1016/j.nucengdes.2016.03.007

Lakshmipathy, S., 2009. Partially Averaged Navier-Stokes Method for Turbulence 1–133.

Lakshmipathy, S., Girimaji, S., 2006. Partially-averaged Navier–Stokes method for turbulent flows: k-ω model implementation. AIAA Pap. 1–15. https://doi.org/doi:10.2514/6.2006-119

Lee, J.R., Kim, J., Song, C.H., 2014. Synthesis of the turbulent mixing in a rod bundle with vaned spacer grids based on the OECD-KAERI CFD benchmark exercise. Nucl. Eng. Des. 279, 3–18. https://doi.org/10.1016/j.nucengdes.2014.03.008

Lumley, J.L., Newman, G.R., 1977. The return to isotropy of homogeneous turbulence. J. Fluid Mech. 82, 161. https://doi.org/10.1017/S0022112077000585

Maday, Y., Patera, A.T., Rønquist, E.M., 1990. An Operator-integration-factor splitting method for time-dependent problems: Application to incompressible fluid flow. J. Sci. Comput. 5, 263–292. https://doi.org/10.1007/BF01063118

Mahaffy, J., Chung, B., Song, C., Dubois, F., Graffard, E., Ducros, F., Heitsch, M., Scheuerer, M., Henriksson, M., Komen, E., Moretti, F., Morii, T., Muehlbauer, P., Rohde, U., Smith, B.L., Watanabe, T., Zigh, G., 2015. Best Practice Guidelines for the Use of CFD in Nuclear Reactor Safety Applications - Revision.

Merzari, E., Fischer, P., Yuan, H., Van Tichelen, K., Keijers, S., De Ridder, J., Degroote, J., Vierendeels, J., Doolaard, H., Gopala, V.R., Roelofs, F., 2016. Benchmark exercise for fluid flow simulations in a liquid metal fast reactor fuel assembly. Nucl. Eng. Des. 298, 218–228. https://doi.org/10.1016/J.NUCENGDES.2015.11.002

Merzari, E., Ninokata, H., 2011. Proper orthogonal decomposition of the flow in a tight lattice rod-bundle. Nucl. Eng. Des. 241, 4621–4632. https://doi.org/10.1016/j.nucengdes.2010.12.005

Nguyen, T., Hassan, Y., 2017. Stereoscopic particle image velocimetry measurements of flow in a rod bundle with a spacer grid and mixing vanes at a low Reynolds number. Int. J. Heat Fluid Flow 67, 202–219. https://doi.org/10.1016/j.ijheatfluidflow.2017.08.011

Nicoud, F., Ducros, F., 1999. Subgrid-scale stress modelling based on the square of the velocity gradient tensor. Flow, Turbul. Combust. 62, 183–200. https://doi.org/10.1023/A:1009995426001

Ohlsson, J., Schlatter, P., Fischer, P.F., Henningson, D.S., 2011. Stabilization of the

Spectral-Element Method in Turbulent Flow Simulations, in: Hesthaven, J.S., Rønquist, E.M. (Eds.), Spectral and High Order Methods for Partial Differential Equations. Springer Berlin Heidelberg, Berlin, Heidelberg, pp. 449–458.

Patera, A.T., 1984. A spectral element method for fluid dynamics: Laminar flow in a channel expansion. J. Comput. Phys. 54, 468–488. https://doi.org/10.1016/0021-9991(84)90128-1

Pope, S.B., 2000. Turbulent Flows. Cambridge University Press, Cambridge. https://doi.org/10.1017/CBO9780511840531

Razi, P., Tazraei, P., Girimaji, S., 2017. Partially-averaged Navier–Stokes (PANS) simulations of flow separation over smooth curved surfaces. Int. J. Heat Fluid Flow. https://doi.org/10.1016/j.ijheatfluidflow.2017.05.005

Reyes, D.A., Cooper, J.M., Girimaji, S.S., 2014. Characterizing velocity fluctuations in partially resolved turbulence simulations. Phys. Fluids 26. https://doi.org/10.1063/1.4892008

Roache, P.J., 1997. QUANTIFICATION OF UNCERTAINTY IN COMPUTATIONAL FLUID DYNAMICS. Annu. Rev. Fluid Mech. https://doi.org/10.1146/annurev.fluid.29.1.123

Schumann, U., 1977. Realizability of Reynolds-stress turbulence models. Phys. Fluids 20, 721–725. https://doi.org/10.1063/1.861942

Simonsen, A.J., Krogstad, P., 2016. Turbulent stress invariant analysis : Clarification of existing terminology Turbulent stress invariant analysis : Clarification of existing terminology 088103, 1–5. https://doi.org/10.1063/1.2009008

Speziale, C.G., 1982. On turbulent secondary flows in pipes of noncircular cross-section. Int. J. Eng. Sci. 20, 863–872. https://doi.org/10.1016/0020-7225(82)90008-8

Todreas, N., Kazimi, M., 2011. Nuclear Systems I Thermal Hydraulic Fundamentals. CRC Press.

Tong, L.S., Weisman, J., 1996. Thermal Analysis of Pressurized Water Reactors. American Nuclear Society.